https://doi.org/10.5194/egusphere-2026-4245
Preprint. Discussion started: 10 August 2026

Using an offline ensemble Kalman filter to estimate ammonia emissions in the Netherlands

Simeng Li[1], Enrico Dammers[1,2], Beatriz Herrera[2], Arjo Segers[2], Mark W. Shephard[3], Martin Van Damme[4,5], Lieven Clarisse[4], Shelley van der Graaf[6], Roy Wichink Kruit[6], and Jan Willem Erisman[1]

[1]Institute of Environmental Sciences, Universiteit Leiden, Leiden, the Netherlands
[2]Air Quality and Emissions Research, Netherlands Organisation for Applied Scientific Research (TNO), Utrecht, The Netherlands
[3]Environment and Climate Change Canada, Toronto, Ontario, Canada
[4]Spectroscopy, Quantum Chemistry and Atmospheric Remote Sensing (SQUARES), BLU–ULB Space Research Center, Université Libre de Bruxelles (ULB), Brussels, Belgium
[5]Royal Belgian Institute for Space Aeronomy, Brussels, Belgium
[6]Rijksinstituut voor Volksgezondheid en Milieu, RIVM, Bilthoven, the Netherlands

Correspondence: Simeng Li (s.li@cml.leidenuniv.nl)

Abstract. Ammonia (NH_3) emissions from agricultural sources remain highly uncertain, yet accurate emission estimates are essential for assessing impacts on air quality, ecosystem nitrogen deposition, and secondary aerosol formation. In this study, we apply an offline Localised Ensemble Kalman Filter (LEKF), where offline refers to the application of the filter to pre-computed ensemble model output without feeding the analysis back into the running model, to constrain monthly NH_3 emissions over the Netherlands for 2022, using ensemble simulations from the LOTOS-EUROS chemical transport model as the dynamical background. Observations from two complementary data streams are assimilated: ground-based in situ NH_3 concentration measurements from the MAN and LML networks, and satellite column retrievals from CrIS and IASI. The inversion system accounts for observation error characterisation, regularisation to prevent overfitting, and the application of satellite averaging kernels to ensure consistent comparison between retrieved and simulated columns. System performance is evaluated through synthetic perturbation experiments before application to real observations, which reveal systematic discrepancies between the prior inventory and observed concentrations, particularly during summer months when the prescribed emission time profile underestimates ambient NH_3. Finally, we assess observation network optimisation by identifying measurement locations that would maximally improve emission constraints across the Netherlands, providing practical recommendations for future monitoring network design.

1 Introduction

Ammonia, the most abundant alkaline and a highly reactive gas in the atmosphere, poses dual environmental threats: it contributes to particulate matter formation that degrades air quality and threatens human health, while its deposition onto soil and water ecosystems can trigger biodiversity loss and ecological damage (Erisman et al., 2007, 2008, 2013). Gu et al. (2021) demonstrated that nitrogen species accounted for 39% of global $PM_{2.5}$ exposure in 2013, with ammonia's contribution ex-

https://doi.org/10.5194/egusphere-2026-4245
Preprint. Discussion started: 10 August 2026

ceeding that of NO_x globally. Lelieveld et al. (2015) established agriculture as the leading cause of air pollution mortality in Europe, with ammonia from animal husbandry and fertilizers being a particularly effective $PM_{2.5}$ precursor. European-specific assessments indicate that a 50% reduction in agricultural NH_3 emissions could prevent more than 200,000 premature deaths annually (Giannadaki et al., 2018).

Despite decades of scientific attention, significant uncertainties persist regarding ammonia's atmospheric budget, particularly emission quantification. The high solubility and adhesive properties of ammonia, combined with its short atmospheric lifetime and temperature-dependent bidirectional exchange, create substantial challenges for accurately determining emission rates and subsequent deposition patterns (Ge et al., 2023). NH_3 presents unique modelling challenges due to its short and variable atmospheric lifetime (12–48 hours on average), driven by bidirectional surface–atmosphere exchange, dry deposition, and particle-phase partitioning (Pai et al., 2021). Wang et al. (2025) demonstrated that global mean lifetime estimates of approximately 2 days mask substantial regional variability, with model-to-model differences in total NH_3 reaching a factor of 17 globally, with direct influences for SNA (sulfate–nitrate–ammonium aerosols) and $PM_{2.5}$ prediction. Over Europe, classified as an "NH_3-rich" region, these uncertainties are compounded by complex nonlinear interactions between NH_3, NO_x, and SO_2 that further complicate emission-concentration relationships (Wang et al., 2025).

Top-down approaches, particularly inverse modeling techniques, have become essential tools for constraining ammonia emissions from observational data. The Ensemble Kalman filter (EnKF) framework (Evensen, 2003) offers particular advantages for emission inversion problems. By propagating ensembles through an atmospheric model, it naturally accommodates nonlinear emission-concentration relationships. Moreover, it circumvents the need to explicitly construct and store tangent linear (Jacobian) and prior covariance matrices, which reduces computational overhead. To name a few, van der Graaf et al. (2022) demonstrated the Local Ensemble Transform Kalman Filter (LETKF) application for European NH_3 emissions, assimilating Cross-track Infrared Sounder (CrIS) satellite retrievals into LOTOS-EUROS and finding required emission increases of up to 30%. Kong et al. (2019) applied EnKF to Chinese ground-based passive sampler observations at monthly resolution, revealing posterior emissions exceeding priors by more than a factor of 2 in northwestern regions.

More recently, Ding et al. (2024) applied the Daily Emissions Constrained by Satellite Observations (DECSO) algorithm to CrIS and TROPOMI observations to estimate NH_3 and NO_x emissions over Europe, showing good consistency with independent bottom-up inventories. And Xia et al. (2025) conducted South Asian emission inversions using Infrared Atmospheric Sounding Interferometer (IASI) satellite observations, demonstrating the continued value of combining satellite retrievals with advanced data assimilation frameworks.

There are many studies regarding satellite-based inverse modeling of ammonia emissions (Dammers et al., 2019; van der Graaf et al., 2022; Xia et al., 2025; Chen et al., 2026); however, investigations systematically integrating multiple observation types, particularly combining satellite retrievals with ground-based in situ measurements, remain scarce. In the Netherlands, the MAN (Measuring Ammonia in Nature) network provides extensive spatial coverage with monthly passive samplers at over 200 locations (Lolkema et al., 2015), complemented by hourly optical measurements from the LML (Landelijk Meetnet Luchtkwaliteit) network (Berkhout et al., 2017). Despite this rich observational infrastructure, systematic evaluation of network adequacy for emission inversion applications has been limited. Li et al. (2025) demonstrated successful local-scale inversion

https://doi.org/10.5194/egusphere-2026-4245
Preprint. Discussion started: 10 August 2026

using MAN observations, but questions remain regarding optimal integration strategies and network sufficiency at regional scales.

This study develops an offline Localised Ensemble Kalman Filter (LEKF-Offline) to address these questions. In contrast to an online implementation, where the assimilated state is fed back into the running model at each cycle, the offline approach applies the Kalman filter to pre-computed ensemble model output without modifying the forward model trajectory. This design decouples the inversion from the model runtime, making the system computationally tractable while retaining the full ensemble-based uncertainty quantification of the standard EnKF framework. The LEKF-Offline is driven by ensemble simulations from the LOTOS-EUROS chemical transport model and is used to systematically evaluate emission inversion performance across multiple observation configurations: (1) in situ measurements alone (MAN and LML), (2) satellite observations (CrIS and IASI) alone, (3) combined satellite and ground-based observations, and (4) integration with hourly LML measurements. Through Observing System Simulation Experiments (OSSEs) with known emission perturbations, we assess:

- Comparative performance of satellite-only versus ground-based-only versus combined observation inversions.
- Optimal observational configurations for constraining monthly emission estimates.
- Network adequacy for detecting emission changes at magnitudes relevant to potential Dutch policy targets.
- Temporal scale dependencies in constraint capability, from daily to seasonal timescales.

The LEKF-Offline framework addresses key methodological challenges including regularisation strategies for handling the over-determined system created by monthly averaged satellite overpasses constraining monthly emissions, iterative treatment of emission-concentration nonlinearities, and integration of observation types with vastly different spatial coverage, temporal resolution, and error characteristics. Our results provide guidance for optimizing ammonia monitoring strategies in regions requiring robust emission verification systems.

2 Data and Methodology

2.1 Experimental setup and time series definition

This study focuses on NH_3 emission inversion over the Netherlands for the year 2022, selected as a representative year with sufficient observational coverage from both ground-based networks and satellite instruments. Emissions are estimated at monthly resolution, with one inversion cycle performed per month, yielding twelve independent posterior emission scaling factor fields over the study period.

The inversion system follows an offline design, in contrast to online data assimilation where observations are assimilated sequentially and the updated state is propagated forward in time. In the offline approach, a pre-computed ensemble of perturbed annual LOTOS-EUROS simulations is used to construct the forecast error covariance, and each monthly posterior state vector is estimated independently without sequential state propagation. This design decouples the inversion from the forward model

https://doi.org/10.5194/egusphere-2026-4245
Preprint. Discussion started: 10 August 2026

runtime, making the system computationally tractable for the large number of satellite observations assimilated here, while retaining the ensemble-based uncertainty quantification of the standard EnKF framework.

2.2 Observations

2.2.1 In situ measurements

The MAN network provides widespread ammonia monitoring across the Netherlands using passive samplers, offering a cost-effective and easily deployable measurement approach (site locations shown in Fig. 1 Lolkema et al., 2015; Noordijk et al., 2020). While the MAN network provides substantially denser spatial coverage compared to high-precision optical instruments, the measurements are characterized by larger uncertainties. These uncertainties arise from multiple sources, including random measurement variability, calibration methods, calibration standard (Lolkema et al., 2015; Noordijk et al., 2020).

The Landelijk Meetnet Luchtkwaliteit (LML) network (Berkhout et al., 2017; van Zanten et al., 2017) provides complementary high-temporal-resolution ammonia observations at hourly intervals using miniDOAS (mini Differential Optical Absorption Spectroscopy) optical instruments. These measurements offer higher precision than passive samplers but are deployed at fewer locations due to instrumental costs and operational requirements.

2.2.2 Satellite products

This study incorporates total column NH_3 retrievals from two infrared satellite instruments, CrIS and IASI, to constrain monthly emission estimates over the Netherlands. Pre-gridded products are used rather than individual pixel retrievals: for each overpass, the averaging kernel (AVK) is applied to the corresponding LOTOS-EUROS model profile interpolated to the satellite pixel location, yielding a model-equivalent column that accounts for the vertical sensitivity of the retrieval. The AVK-smoothed model equivalents and the associated retrieval uncertainties are then aggregated spatially onto the model grid and averaged over each month to produce the monthly observational dataset used in the inversion. Retrieved data are restricted to land grid cells only, and quality filtering is applied prior to averaging as described below for each instrument.

CrIS (Cross-track Infrared Sounder, Shephard and Cady-Pereira, 2015; Shephard et al., 2020; White et al., 2023) is a Fourier transform spectrometer on board the polar-orbiting Suomi-NPP, NOAA-20, and NOAA-21 satellites, launched in 2011, 2017, and 2022, respectively. Daytime overpasses occur at approximately 13:30 local time (LT), providing daily coverage over the study domain. CrIS scans a 2200 km swath with a nadir pixel size of approximately 14 km. We apply stringent quality filters to ensure reliable retrievals: only daytime observations with high retrieval quality (`Quality Flag` ≥ 3) and relatively clear-sky conditions (`Cloud Flag` $= 1$) are retained. The averaging kernel for CrIS is a full two-dimensional matrix, applied with explicit departure from the a priori profile x_a:

$$\hat{y} = \sum_i \left[x_a^i + \sum_j A_{ij} \left(x_{\text{model}}^j - x_a^j \right) \right] h_T^i \tag{1}$$

where x is the model profile, x_a is the retrieval a priori profile, A_{ij} is the linear averaging kernel matrix, and h_T^i is the pressure-weighted air mass factor converting units to molecules cm^{-2}.

https://doi.org/10.5194/egusphere-2026-4245
Preprint. Discussion started: 10 August 2026

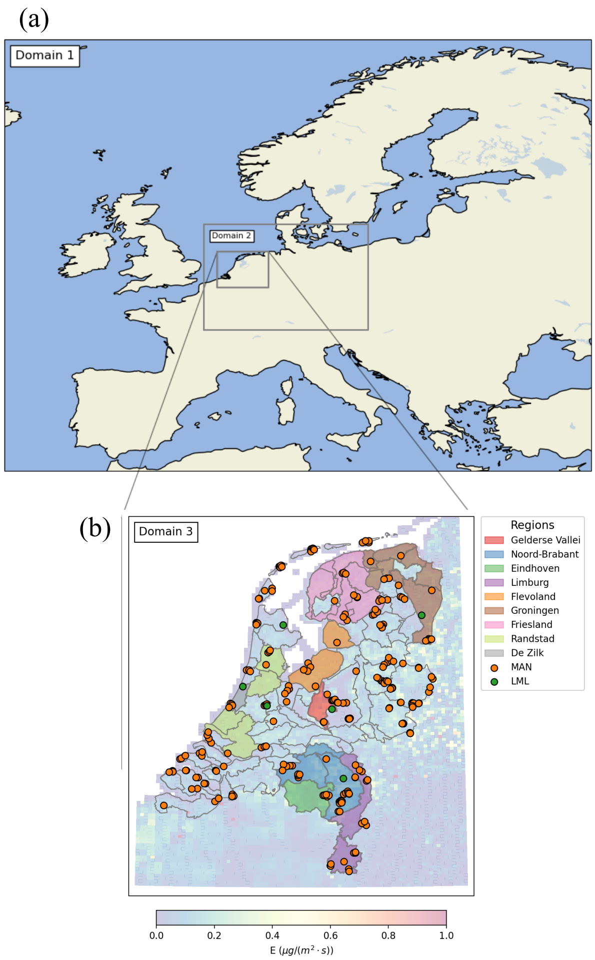

Figure 1. (a) Nested domain configuration for the LOTOS-EUROS simulation. In Domain 3 (panel b), orange circles denote MAN measurement sites, and green circles denote LML sites. Coloured shading indicates the regions referenced in the text; the background field shows the annual mean NH_3 emission (μg m^{-2} s^{-1}).

IASI (Infrared Atmospheric Sounding Interferometer, Clerbaux et al., 2009; Van Damme et al., 2017; Clarisse et al., 2023) is a Fourier transform spectrometer on board the MetOp satellite series (MetOp-A/B/C, launched in 2006, 2012, and 2018, respectively). Daytime overpasses occur at approximately 09:30 LT, providing daily global coverage. IASI scans a 2200 km swath with a nadir pixel size of approximately 12 km. Data filtering retains only daytime observations with limited cloud contamination. For IASI, a one-dimensional column averaging kernel is provided that implicitly accounts for the a priori contribution and is applied directly as (Clarisse et al., 2023):

$$\hat{y} = \sum_{i} A^{j} \cdot x^{j}_{\text{model}} \tag{2}$$

https://doi.org/10.5194/egusphere-2026-4245
Preprint. Discussion started: 10 August 2026

Table 1. LOTOS-EUROS model configuration

Parameters	Setting	Notes/Citation
Time period	January 1 to December 31, 2022	with a spin-up for 15 days
Spatial resolution	0.05° × 0.025°	3.6 km × 4.3 km
Region	(50.65°N, 3.15°E) to (53.7°N, 7.5°E)	87 × 122 grid cells
Emission	CAMS-REG v5.1 REF2 for the Domain 1, GrETa and ER for Domain 2 & 3	Kuenen et al. (2022), year 2019
Meteorology	ECMWF Reanalysis v5 (ERA5)	Hersbach et al. (2020)

For spatial resolution, the first and second column denote (Δlon $\times$ Δlat) and ($\Delta x \times \Delta y$), respectively.

where A^j is the column averaging kernel and x^j_{model} is the modelled partial column in layer j. The difference in averaging kernel conventions between the two products reflects their distinct retrieval methodologies and may contribute to systematic differences in the model-equivalent simulations (Sect. 3.2).

The combined use of CrIS and IASI provides dense spatial and temporal observational coverage for monthly emission inversions. The large number of satellite observations relative to the degrees of freedom in the state vector creates a potentially overdetermined system; this is addressed through regularisation (Sect. 2.4).

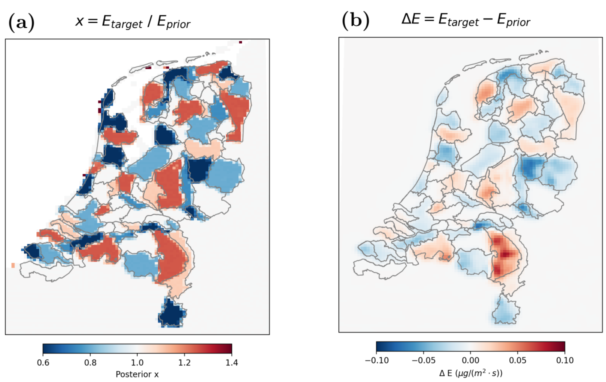

Figure 2. Target state vector (a) and the absolute NH_3 emission changes (b) applied in the multi-perturbation experiment using the Panorama Landschap regional classification (Rijksdienst voor het Cultureel Erfgoed, 2026).

2.2.3 Synthetic observations

We validate the offline LEKF using synthetic observations generated by LOTOS-EUROS within an Observing System Simulation Experiment (OSSE) framework. The validation first employs a uniform 40% emission reduction applied to all grid cells and months, creating a known target scaling factor of 0.6 against which inversion performance is evaluated.

https://doi.org/10.5194/egusphere-2026-4245
Preprint. Discussion started: 10 August 2026

To assess the system's capability to resolve spatially heterogeneous emissions at sub-provincial scales, we implement a multi-perturbation experiment using the Panorama Landschap regional classification (Rijksdienst voor het Cultureel Erfgoed, 2026), which divides the Netherlands into 78 distinct landscape regions characterised by coherent land use patterns and agricultural practices. The resulting target pattern, shown in Fig. 2, spans scaling factors from 0.6 (40% emission reduction) to 1.4 (40% emission increase). This experiment applies spatially varying emission perturbations across different landscape regions, allowing us to evaluate whether the existing monitoring network configuration can adequately constrain emissions in areas with strong spatial variability.

Synthetic in situ measurements are similarly derived from the perturbed model output, with added Gaussian noise representative of the measurement uncertainty characterising each network. Synthetic satellite observations are constructed using the LOTOS-EUROS perturbed simulation as the true state, with averaging kernels set to unity at every vertical level. Although this assumption is optimistic relative to real retrieval conditions, it provides an upper bound on the system's theoretical performance and isolates the limitations arising from the inversion framework itself rather than from retrieval sensitivity.

2.3 LOTOS-EUROS

In this study, we employ LOTOS-EUROS (LOng-Term Ozone Simulation and European Operational Smog model) version 2.3.000 (Manders et al., 2017; Manders-Groot and LOTOS-EUROS team, 2023) as the forward model for both generating synthetic observations and running ensemble simulations within the inversion framework. Developed by TNO, LOTOS-EUROS is a state-of-the-art regional air quality model that integrates atmospheric transport, chemical transformation, and deposition processes relevant to ammonia. The model is driven by meteorological fields from the European Centre for Medium-Range Weather Forecasts (ECMWF) reanalysis v5(Hersbach et al., 2020). Three-hourly meteorological parameters are temporally interpolated to one-hour resolution to provide finer temporal representation of atmospheric dynamics. To balance computational efficiency with spatial detail, we implement a nested domain configuration (Fig. 1). The finest domain focuses on the Netherlands, covering (50.65°N, 3.15°E) to (53.7°N, 7.5°E) at $0.05° \times 0.025°$resolution at approximately 3.6 km $\times$ 4.3 km resolution. This nested approach enables high-resolution simulation over the study region while maintaining appropriate boundary conditions from the larger European domain. More details can be found in Table 1.

2.4 Localised Ensemble Kalman Filter – Offline Implementation

To integrate satellite and ground-based MAN measurements for emission estimation, we develop an offline Localized Ensemble Kalman Filter (LEKF-Offline) using ensemble output from LOTOS-EUROS. The ensemble approach propagates emission uncertainties through the model, avoiding the need to explicitly construct Jacobian matrices or prior error covariance structures (Evensen, 2003). In contrast to online data assimilation, where observations are assimilated sequentially and the updated state is propagated forward in time, the offline formulation employed here uses a pre-computed ensemble of perturbed annual simulations to invert monthly emissions independently, with each monthly posterior state vector estimated separately without sequential state propagation.

https://doi.org/10.5194/egusphere-2026-4245
Preprint. Discussion started: 10 August 2026

The analysis update follow the standard EnKF framework:

$$\boldsymbol{x}_i^a = \boldsymbol{x}_i^f + \mathbf{K}\left(\boldsymbol{y}^o - \mathbf{H}\boldsymbol{x}_i^f + \boldsymbol{v}_i\right) \tag{3}$$

where $\boldsymbol{x}_i^a$ and $\boldsymbol{x}_i^f$ represent the analysis (posterior) and forecast (prior) ensemble members, respectively; $\mathbf{K}$ is the Kalman gain; $\boldsymbol{y}^o$ is the observation vector; $\mathbf{H}$ is the observation operator; and $\boldsymbol{v}_i \sim \mathcal{N}(\mathbf{0}, \mathbf{R})$ represents perturbed observation errors drawn for each ensemble member, where $\mathbf{R}$ is the observation error covariance matrix. The Kalman gain is given by:

$$\mathbf{K} = \mathbf{P}^f\mathbf{H}^T\left[\mathbf{H}\mathbf{P}^f\mathbf{H}^T + \frac{1}{\gamma}\mathbf{R}\right]^{-1} \tag{4}$$

where $\mathbf{P}^f$ is the forecast ensemble covariance matrix; the regularisation parameter $\gamma \in (0,1)$ effectively reduces observational weight in the analysis, which is optimised and described in Sect. 2.4.3. Detailed mathematical derivations are provided in Appendix A.

2.4.1 Covariance localisation

With a limited ensemble size, the sample-based forecast error covariance matrix $\mathbf{P}^f$ inevitably contains spurious long-range correlations that can degrade the analysis update. To suppress these, we apply a distance-dependent localisation function that tapers the covariance to zero beyond a prescribed length scale ρ.

The choice of $\rho = 15$ km is informed by a spatial correlation analysis of the MAN ground-based network (255 sites, 2010–2023), presented in Fig. A1. Measured NH_3 concentrations across MAN sites are highly correlated at distances well exceeding the Netherlands domain (∼300 km), reflecting the dominance of the shared seasonal cycle and interannual common signals rather than spatially resolved emission structure. After removing both the monthly climatology and the network-wide spatial mean, the residual local anomalies decay rapidly with distance, crossing zero at approximately 107 km. Fitted exponential and Gaussian decay functions yield correlation lengths of $\rho = 17 \pm 3$ km and $\rho = 15 \pm 3$ km, respectively. The localisation radius is therefore set to $\rho = 15$ km, corresponding to a Gaussian cutoff factor of 3.5.

This decomposition also reveals an important limitation of the MAN network: the local anomalies remaining after signal removal are characterised by large random variability and weak spatial structure, suggesting that MAN observations carry limited information about fine-scale emission gradients at the sub-provincial level. This is discussed further in Sect. 3.3.

2.4.2 Observation error characterisation

For the observations, we construct the observational error with two components (Eq. 5). For in situ observations, the measurement error $\varepsilon_{\text{measurement}}$ is taken from the reported uncertainties. And for satellite observations, $\varepsilon_{\text{measurement}}$ is taken directly from the retrieval uncertainty provided with each CrIS and IASI product, representing the random instrumental error. The residual error $\varepsilon_{\text{residual}}$ is derived from the spread of observation-minus-model innovations across the ensemble, after removing the ensemble mean misfit, and therefore characterises the combined effect of model structural uncertainty and representativeness error rather than the retrieval smoothing error. Since satellite averaging kernels are explicitly applied within the observation

https://doi.org/10.5194/egusphere-2026-4245
Preprint. Discussion started: 10 August 2026

operator, the smoothing error is already accounted for in the model-equivalent simulations and is not included separately in the observational error covariance matrix.

Following Li et al. (2025), we apply χ^2 statistical tests to optimise the scaling factor α, which controls the relative contribution of the measurement error to the total observational error covariance. Specifically, the observational error vector is formulated as:

$$\varepsilon = \sqrt{\varepsilon_{\text{residual}}^2 + (\alpha \cdot \varepsilon_{\text{measurement}})^2} \tag{5}$$

where $\varepsilon_{\text{residual}}$ is the spread of observation-minus-model innovations across the ensemble and $\varepsilon_{\text{measurement}}$ is the measurement error. Note that α is distinct from the regularisation parameter γ introduced in Sect. 2.4.3: while α scales the observation error in the $\mathbf{R}$ matrix, γ dampens the Kalman gain to prevent overfitting. Both parameters are optimised but act on different components of the inversion system. Through this optimisation, we determine $\alpha = 0.15$ for satellite data and $\alpha = 0.3$ for in situ MAN measurements (Li et al., 2025). Additional details are provided in Appendix B.

The dual optimisation strategy addresses both error characterisation and overfitting: χ^2 testing ensures statistically consistent observation errors (α optimisation), while regularisation (γ optimisation) prevents numerical instabilities arising from the severely over-determined system when monthly averaged total column observations constrain monthly emissions.

2.4.3 Regularisation for satellite observations

When assimilating monthly averaged satellite total column retrievals to constrain monthly emissions, the system becomes severely overdetermined: the number of observations (9674–9993 per month, depending on the satellite and month) far exceeds the ensemble size ($m = 12$), leading to overfitting and numerical instabilities in the Kalman gain computation. Following Lu et al. (2021), we implement regularisation by inflating the observation error covariance:

We determine γ by requiring the analysis increment to satisfy χ^2 statistical criteria. Specifically, the state-space cost function:

$$\mathcal{J}_A = \left(\boldsymbol{x}^a - \boldsymbol{x}^f\right)^T \left(\mathbf{P}^f\right)^{-1} \left(\boldsymbol{x}^a - \boldsymbol{x}^f\right) \tag{6}$$

should approximate the number of state parameters: $\mathcal{J}_A \approx n \pm \sqrt{2n}$ for an optimally balanced system with n emission parameters, in which $\mathbf{P}^f$ is the forecast ensemble covariance matrix including localisation.

For monthly in situ observations, no regularisation is necessary ($\gamma = 1.0$) since the temporal aggregation naturally matches the monthly emission timescale and the number of observations does not lead to overfitting. For satellite observations, however, the large number of column retrievals relative to the ensemble size produces moderate overfitting without regularisation ($\mathcal{J}_A \approx 3.5n$). Through systematic χ^2 testing (Fig. 3a), an optimal regularisation parameter is identified for each month and satellite product independently, targeting $\mathcal{J}_A \approx n$. The optimised γ values range from 0.01 to 0.5 and are provided in Table S1. CrIS retrievals consistently require stronger regularisation (γ as low as 0.01 during spring and summer) compared to IASI (γ ranging from 0.05 to 0.3), reflecting the larger random variability in the CrIS product visible in Fig. 7. Both instruments require stronger regularisation in winter months (November–January), consistent with increased retrieval uncertainty due to reduced thermal contrast and cloud contamination during this season.

https://doi.org/10.5194/egusphere-2026-4245
Preprint. Discussion started: 10 August 2026

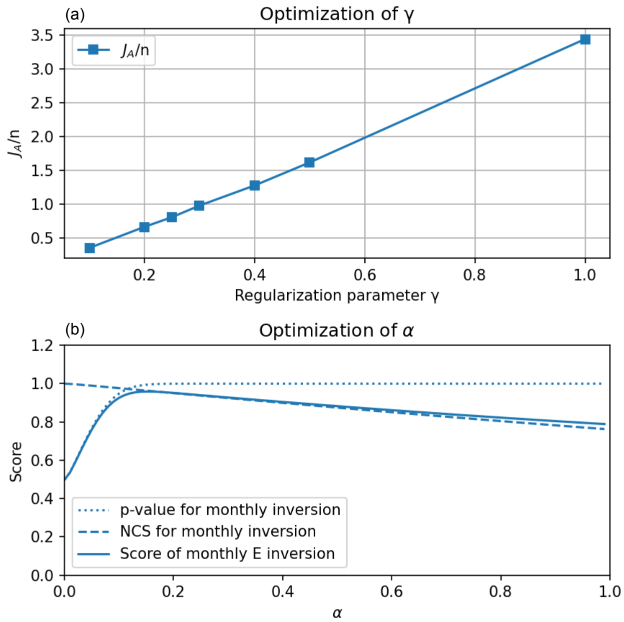

Figure 3. Optimisation of α and γ for satellite observations through χ^2 testing. The selected values $\alpha = 0.15$ and $\gamma = 0.1$ achieve statistical balance with $\mathcal{J}_A \approx n$. The results for the MAN measurement could be found in the supplement.

Table 2. Overview of observational configurations tested in simulated and real data experiments. Checkmarks ($\times$) indicate datasets included in each configuration. Each row represents a unique combination of observational datasets assimilated in the LEKF-Offline system. Figure references indicate where results are presented for synthetic observation experiments (Sect. 3.1) and real observation inversions (Sect. 3.2). The LML-only configuration is not performed due to the limited spatial coverage of the LML network across the Netherlands.

Configuration	MAN	LML	CrIS	IASI	Synthetic obs.	Real obs.
MAN only	$\times$				Fig. S2 , S3	Fig. S13
MAN + LML	$\times$	$\times$			Fig. 4a , 5a	Fig. 6a
CrIS only			$\times$		Fig. S4 , S5	Fig. S14
IASI only				$\times$	Fig. S6 , S7	Fig. S15
CrIS + IASI			$\times$	$\times$	Fig. 4b , 5b	Fig. 6b
All combined	$\times$	$\times$	$\times$	$\times$	Fig. 4c , 5c	Fig. 6c

When assimilating in situ and satellite observations simultaneously, the regularisation is applied independently to each data stream prior to concatenation. The normalised observation error vector for each data type is scaled by its respective regularisation parameter as $\varepsilon/\sqrt{\gamma}$, and the scaled vectors are concatenated into a single observation array. This approach allows different regularisation strengths to be applied to structurally different observation types within a single analysis step.

https://doi.org/10.5194/egusphere-2026-4245
Preprint. Discussion started: 10 August 2026

2.4.4 Degrees of freedom for signal and observation effectiveness

The degrees of freedom for signal (DFS) quantifies the independent information content extracted from observations by the inversion system. In state vector space, DFS is defined as:

$$\mathrm{DFS} = \mathrm{tr}(\mathbf{A}) = \mathrm{tr}\left[\mathbf{I} - \mathbf{P}^a \left(\mathbf{P}^f\right)^{-1}\right] \tag{7}$$

where $\mathbf{A}$ is the averaging kernel matrix, $\mathbf{P}^f$ is the forecast error covariance matrix, and $\mathbf{P}^a$ is the posterior error covariance matrix. The computation of $\mathbf{P}^f$ and $\mathbf{P}^a$ from the ensemble is detailed in Appendix A. A higher DFS indicates that the observations effectively reduce uncertainty in the emission state vector.

The observation effectiveness quantifies the contribution of individual observations to the posterior update in observation space:

$$\frac{\partial \hat{\boldsymbol{y}}}{\partial \boldsymbol{y}} = \mathbf{HK} = \mathbf{HP}^f\mathbf{H}^T\left[\mathbf{HP}^f\mathbf{H}^T + \mathbf{R}\right]^{-1} \tag{8}$$

following Li et al. (2025), where the diagonal elements of $\mathbf{HK}$ represent the effectiveness of each individual observation, and HK-DFS $= \mathrm{tr}(\mathbf{HK})$. These diagnostics are applied in Sect. 3.3 to evaluate the spatial distribution of observation information content and to identify locations where additional monitoring would most effectively constrain NH_3 emission estimates.

3 Results

For clarity of presentation, seasonal posterior emission fields are discussed in the main text, computed as the average of monthly posterior emissions weighted by the respective emission scaling factors: winter (DJF), spring (MAM), summer (JJA), and autumn (SON). Full monthly results for the state vector are provided in the Supplement, and the complete configuration of all assimilation experiments is summarised in Table 2.

3.1 Synthetic observation experiments

To assess the performance of the LEKF-Offline system, we conduct experiments using synthetic observations under two controlled perturbation scenarios. The first is a uniform 40% emission reduction applied to all grid cells and all months, yielding a domain-wide target scaling factor of 0.6. The second is a spatially heterogeneous multi-perturbation scenario, in which different regions of the Netherlands are assigned distinct scaling factors ranging from 0.6 to 1.4 (Fig. 2), designed to test the system's ability to resolve sub-provincial emission heterogeneity.

Results are presented for three observational configurations: in situ measurements only (MAN+LML), satellite retrievals only (CrIS+IASI), and combined assimilation of all datasets. Results for individual instruments (MAN only, CrIS only, IASI only) are provided in the Supplement. The configuration demonstrating the best performance in the synthetic experiments is subsequently applied to the real-data inversion presented in Sect. 3.2.

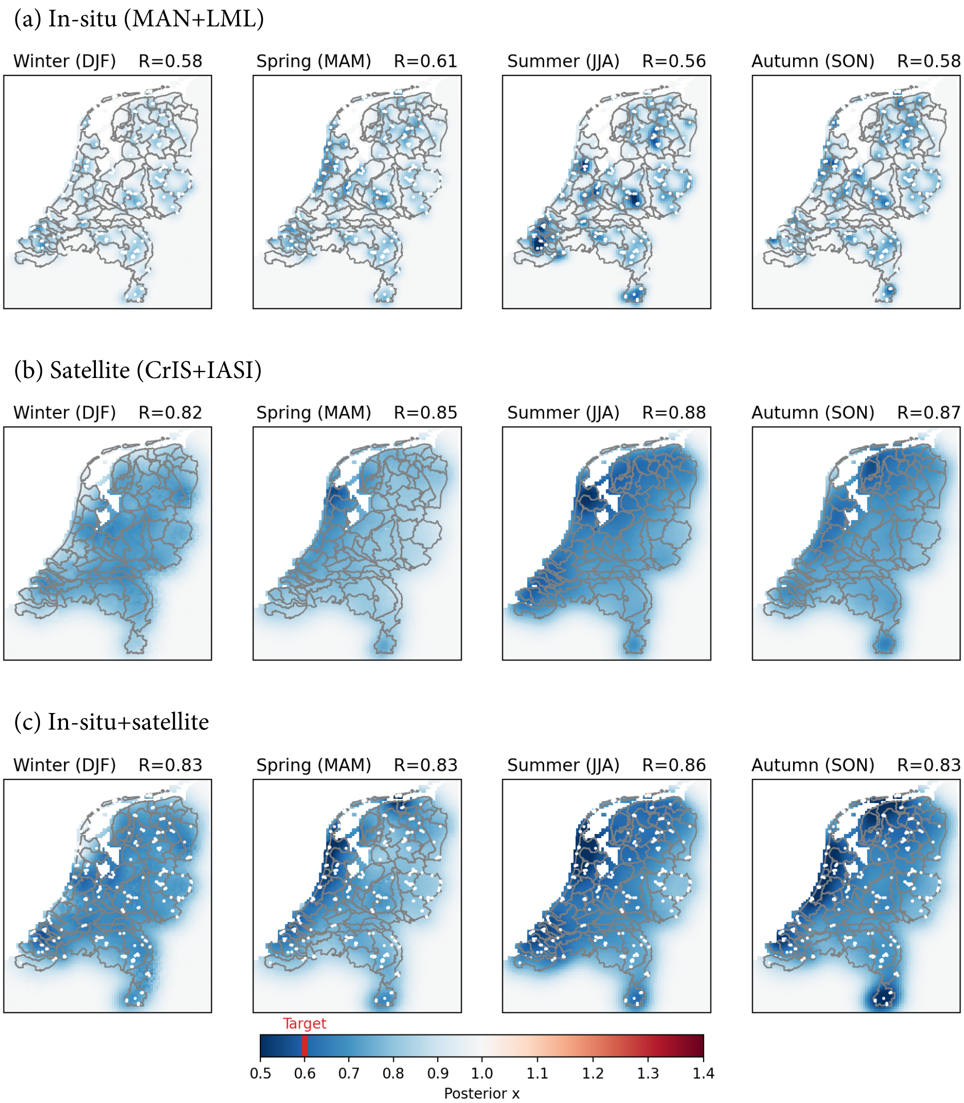

Figure 4. Seasonal posterior emission scaling factors derived from the synthetic uniform 40% emission reduction experiment. White dots indicate in situ station locations. Blue colours indicate emission reductions (scaling factors <1.0) and red colours indicate emission increases (scaling factors >1.0). Experiment configurations are summarised in Table 2.

260 #### 3.1.1 Results with in situ measurements (MAN+LML)

Figure 4(a) shows the seasonal posterior emission scaling factors from the uniform 40% reduction experiment using the combined MAN+LML network. The seasonal structure is consistent with the MAN-only results (Fig. S2), with stronger detection between spring and autumn and weaker adjustments in winter months (January, February, and December), where low ambi-

https://doi.org/10.5194/egusphere-2026-4245
Preprint. Discussion started: 10 August 2026

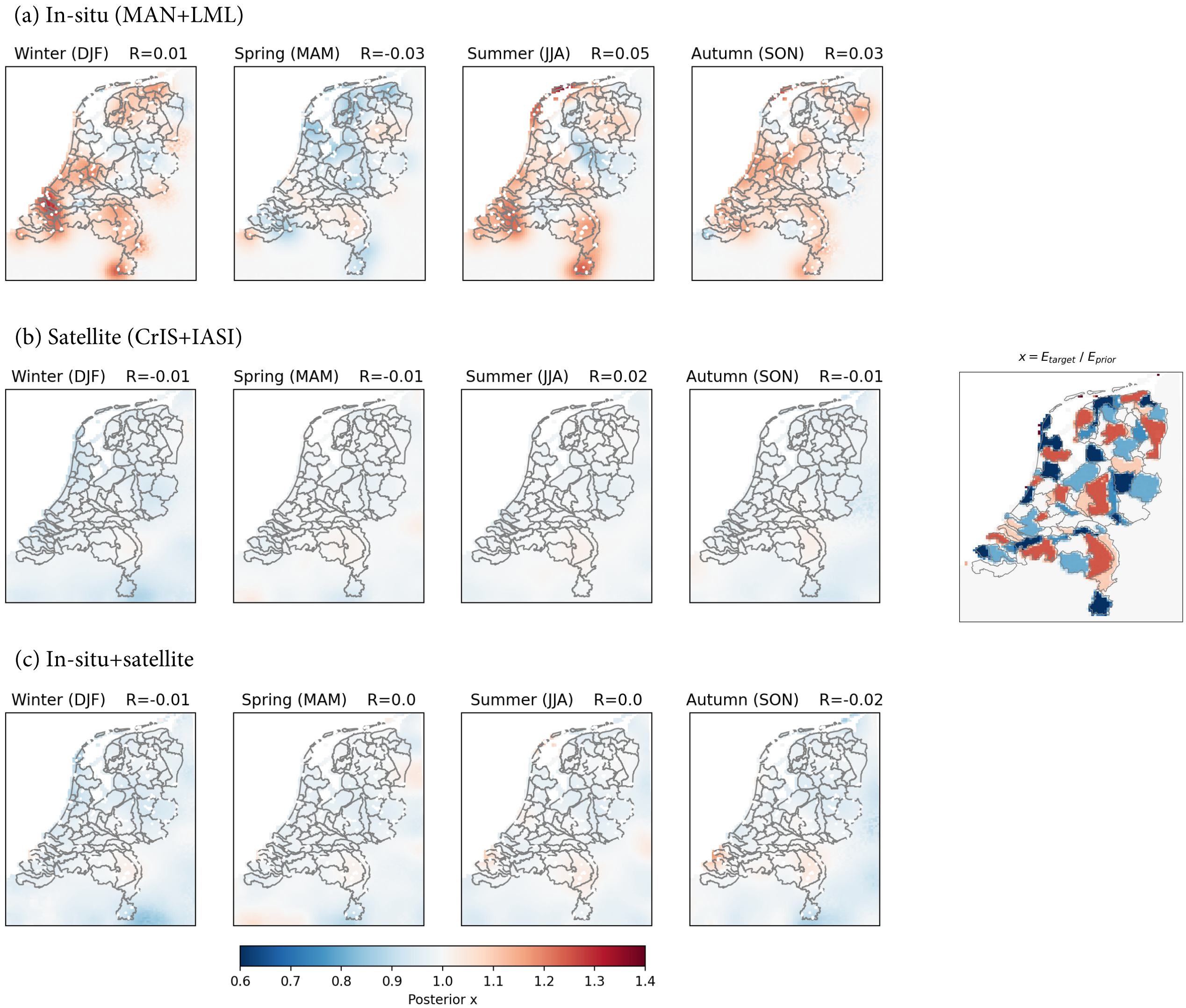

Figure 5. Seasonal posterior emission scaling factors for 2022 derived from synthetic inversion experiments of multi-perturbation (target scaling factors ranging from 0.6 to 1.4; see the right panel and Fig. 2). White dots indicate in situ station locations. Blue colours indicate emission reductions (scaling factors <1.0) and red colours indicate emission increases (scaling factors >1.0). Experiment configurations are summarised in Table 2.

ent NH_3 concentrations limit observation information content. The additional LML stations extend coverage into urban and peri-urban areas not sampled by MAN alone, and the posterior scaling factors show a broader spatial footprint of the detected reduction, particularly in the central Netherlands and Randstad region. Despite this improved coverage, the posterior scaling factors remain systematically above the true value of 0.6 throughout the year as expected, and the residual bias is only

https://doi.org/10.5194/egusphere-2026-4245
Preprint. Discussion started: 10 August 2026

marginally smaller than in the MAN-only case. This indicates that the limiting factor is not station density per se but rather the combined effect of measurement uncertainty.

The multi-perturbation experiment (Fig. 5a) reveals both the strengths and limitations of the combined in situ network more clearly. The system recovers the spatial pattern of imposed perturbations with greater fidelity than the MAN-only configuration (Fig. S3), particularly in regions where LML stations provide local constraint on adjacent emission sources. The influence of individual stations is visible as roughly circular adjustment patterns in the posterior field, reflecting the isotropic Gaussian localisation applied in the LEKF system, whereby each observation constrains the posterior within a circular neighbourhood defined by the localisation radius ($\rho = 15$ km). January and March show the clearest spatial discrimination, with posterior scaling factors reflecting the contrast between reduced and enhanced emission regions in the southwest. During summer months, the spatial structure of the posterior is more diffuse, likely due to increased atmospheric mixing that dilutes the spatial signal of individual source regions. Across most months, posterior values tend to converge toward neutral (0.9–1.1) in areas between station clusters, where the observational constraint is weak.

This homogenisation of the posterior field reflects a fundamental limitation that additional point observations cannot fully overcome: the isotropic 15 km localisation radius does not account for the directional character of NH_3 plume transport, potentially drawing information from upwind locations with little physical connection to the emission sources being adjusted. Although monthly averaging integrates over a range of wind directions and thus partially mitigates this directional bias, the isotropic localisation scheme may still introduce spurious correlations in regions with persistent wind patterns or strong directional emission gradients. A directional localisation scheme incorporating wind field information could better represent the advective relationship between sources and observations and is discussed further in Sect. 3.3.

Taken together, these results confirm that the combined in situ network provides reliable constraints at the domain-to-provincial scale, while resolving sub-provincial emission heterogeneity remains limited by both the observing system geometry and the localisation scheme. It should be noted that the synthetic experiments presented here perturb only NH_3 emissions within the Netherlands, leaving transboundary contributions from neighbouring countries unchanged. In reality, errors in foreign emissions would propagate into the inversion domain as an additional unresolved signal, potentially degrading performance relative to the idealised results shown here.

3.1.2 Results with satellite observations (CrIS+IASI)

Figure 4(b) presents results from the uniform 40% reduction experiment using combined CrIS and IASI satellite observations. The joint assimilation demonstrates notably stronger emission constraints compared to either satellite instrument alone (Figs. S2 and S4). All months show posterior scaling factors predominantly in the 0.6–0.7 range, substantially closer to the target value of 0.6 than the 0.7–0.8 range observed in single-satellite inversions. February, March, June, and September exhibit particularly strong performance, with large areas achieving values near or at the true scaling factor. Even winter months (January and December), which show weaker constraints when using individual instruments, display robust emission reductions throughout the domain. This improved performance reflects the complementary information provided by the two instruments:

https://doi.org/10.5194/egusphere-2026-4245
Preprint. Discussion started: 10 August 2026

their different overpass times, spatial sampling, and retrieval sensitivities combine to provide more comprehensive observational coverage.

Figure 5(b) shows the multi-perturbation experiment results using the combined satellite observations. The joint CrIS–IASI inversion exhibits improved spatial discrimination compared to either instrument individually (Figs. S3 and S5), though spatial patterns remain considerably weaker than the target (Fig. 2). Several regions show discernible structure: Limburg and the Eindhoven area in the southeast display visible emission decreases and increases respectively across multiple months, Flevoland shows modest adjustments, and southwestern coastal regions exhibit detectable patterns. However, the magnitude of these adjustments remains substantially weaker than the imposed perturbations, with most regions showing scaling factors in the 0.9–1.1 range rather than the full 0.6–1.4 range of the target.

These results reveal a fundamental challenge for satellite-only inversions. The regularisation parameter γ, necessary to prevent overfitting given the large number of satellite observations, dampens both the temporal constraint in the uniform case and the spatial gradients in the multi-perturbation case. In addition, satellite column retrievals represent vertically integrated concentrations smoothed by the averaging kernels, which reduces sensitivity to emission variations at landscape scales. The spatial footprint of individual CrIS and IASI pixels (approximately 14 km and 12 km at nadir, respectively) further limits the ability to resolve emission heterogeneity at sub-provincial scales, as each retrieval integrates over an area that may encompass multiple distinct source regions. Atmospheric transport further disperses emission signals over distances comparable to the perturbation scale, reducing the spatial gradients available for the inversion to detect.

Together, these factors explain why the Netherlands, a domain with high spatial emission variability at sub-provincial scales, presents a particularly demanding test for satellite-only inversion. While combined satellite observations effectively constrain large-scale or spatially uniform emission changes, resolving fine-scale heterogeneity likely requires multiple iterations, flow-dependent localisation schemes, or integration with ground-based observations that provide stronger local spatial specificity. Results from individual CrIS and IASI inversions, which exhibit broadly consistent but weaker behaviour, are presented in Figs. S2–S5 in the Supplement.

3.1.3 Results with combined in situ and satellite observations

Figure 4(c) presents the posterior scaling factors from the uniform 40% emission reduction experiment using combined in situ (MAN+LML) and satellite (CrIS+IASI) observations, where all observation types are assimilated simultaneously in a single analysis step. The joint inversion yields an improved constraint relative to either observation type alone, with posterior scaling factors more closely approaching the target value of 0.6 across most of the domain. However, the combined system shows a slight tendency toward overfitting in some regions, where posterior scaling factors fall below the target, reaching values of approximately 0.5 in certain months. This suggests that while the simultaneous assimilation of heterogeneous observation types strengthens the overall emission constraint, the combined system is more sensitive to observation errors, and the regularisation applied here may require further tuning to prevent excessive adjustment beyond the true perturbation magnitude.

Figure 5(c) presents the combined in situ and satellite posterior scaling factors for the multi-perturbation case. The spatial patterns remain broadly consistent with the satellite-only results (Fig. 5b), reflecting the continued dominance of satellite

https://doi.org/10.5194/egusphere-2026-4245
Preprint. Discussion started: 10 August 2026

observations in constraining the posterior at the domain scale. Notably, however, the anomalous large-scale increase visible in March in the satellite-only inversion (Fig. 5b) is absent in the combined result, suggesting that the in situ measurements provide a stabilising constraint that suppresses spurious adjustments driven by satellite retrieval artefacts or localised data quality issues in that month.

Resolving sub-provincial emission heterogeneity remains challenging in the combined inversion, consistent with the findings above. Nevertheless, the integration of in situ observations reduces the posterior uncertainty associated with the satellite-only inversion, particularly in regions with dense ground-based monitoring coverage, where the two data streams provide complementary constraints on local emission patterns.

3.2 Real observations experiments

This section presents posterior emission scaling factors derived from real observations, organised into three parts: in situ measurements (MAN+LML) only, satellite observations (CrIS+IASI) only, and the combined assimilation of all data streams. Results from individual instruments (CrIS alone and IASI alone) are provided in the supplement.

3.2.1 Results with in situ measurements (MAN+LML)

Figure 6(a) presents the spatial distribution of the posterior state vector for ammonia emissions across the Netherlands for each month of 2022, following inversion with real in situ measurements (MAN+LML). The posterior state vector represents the ratio between the optimised (posterior) and prior emission estimates, where values greater than 1 indicate upward adjustments from the prior, values less than 1 indicate downward adjustments, and values near 1 indicate minimal change.

The seasonal maps reveal substantial spatiotemporal variability in emission adjustments. Spring months (March and April) and September show predominantly downward corrections across most of the domain, with April exhibiting particularly strong reductions in eastern and central regions. May through August and October display mixed patterns, with downward adjustments in eastern and southern regions and upward corrections along coastal areas. These spatiotemporal variations reflect the system's response to discrepancies between the prior emission inventory and observed ammonia concentrations, likely capturing the combined influence of seasonal agricultural activities, meteorological variability, and inventory uncertainties.

Two features of the posterior emission warrant further interpretation. First, the prior emission time profile applied here is monotonic, with peak emissions in spring driven by manure application, followed by a relatively flat distribution for the remainder of the year (Manders et al., 2017; Li et al., 2025). In reality, however, ambient ammonia concentrations exhibit a secondary summer peak (Fig. A1b), which the prior does not capture. The posterior adjustments during summer months may therefore partly reflect this temporal misallocation in the emission inventory rather than true changes in yearly total emissions. Second, the pronounced coastal–inland contrast in the posterior scaling factors may reflect systematic differences between MAN measurements and modelled concentrations in coastal grid cells, where sea-breeze dynamics and lower background emissions can introduce biases not fully accounted for in the prior or observation error characterisation.

https://doi.org/10.5194/egusphere-2026-4245
Preprint. Discussion started: 10 August 2026

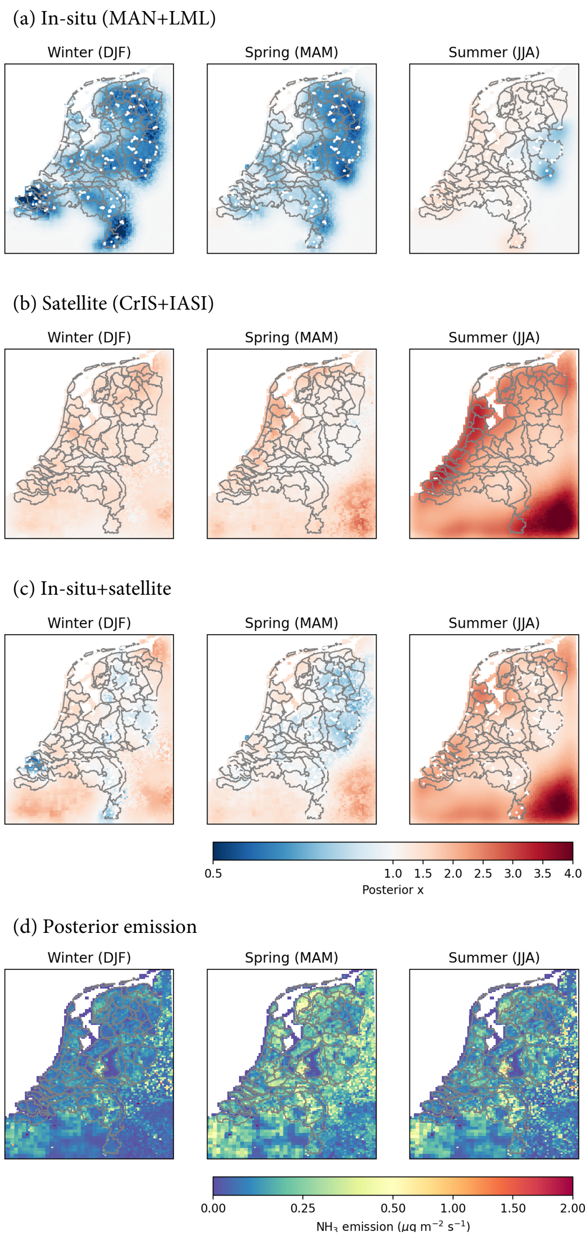

Figure 6. Seasonal posterior emission scaling factors and posterior emission rates for 2022 derived from real observations. Panels (a)–(c) show posterior scaling factors (unitless) for in situ only (MAN+LML), satellite only (CrIS+IASI), and combined in situ and satellite observations, respectively. Blue colours indicate emission reductions (scaling factors <1.0) and red colours indicate emission increases (scaling factors >1.0). Panel (d) shows the posterior emission rate derived from the combined assimilation of all observations; note that the colour scale is nonlinear. Experiment configurations are summarised in Table 2.

https://doi.org/10.5194/egusphere-2026-4245
Preprint. Discussion started: 10 August 2026

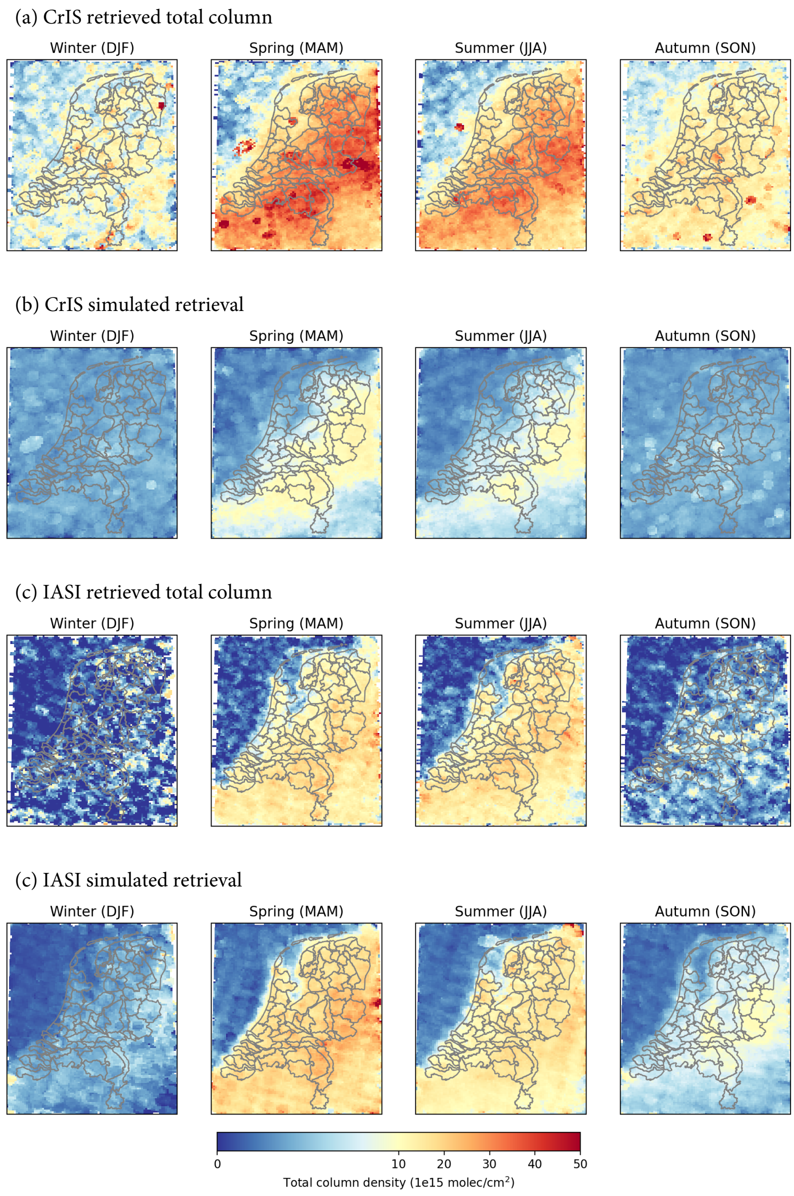

Figure 7. Seasonal NH_3 total column retrievals and prior model-simulated retrievals (with averaging kernels applied) for CrIS (a,b) and IASI (c,d) for 2022. Retrieved columns (a,c) are compared against LOTOS-EUROS simulations convolved with the respective averaging kernels (b,d) to ensure a consistent comparison. Units are 10^{15} molecules cm^{-2}.

https://doi.org/10.5194/egusphere-2026-4245
Preprint. Discussion started: 10 August 2026

3.2.2 Results with satellite observations (CrIS+IASI)

Figure 7 presents the seasonal NH_3 total column retrievals from CrIS and IASI alongside the prior LOTOS-EUROS simulations smoothed with the respective averaging kernels; the corresponding scatter plot for statistical comparison could be found in Fig. S17. Both instruments and the model share consistent spatial and temporal patterns: inland regions exhibit higher column abundances than coastal areas, reflecting the distribution of agricultural emission sources, and the seasonal cycle is dominated by elevated columns in March and April during the spring manure application period, with a modest secondary increase in July and August.

For CrIS (Fig. 7a,b), the retrieved columns are systematically and substantially higher than the model-simulated equivalents throughout the year. The magnitude of this discrepancy may reflect a systematic underestimation of NH_3 emissions in the prior inventory, an issue with the CrIS averaging kernel application, or a diurnal sampling effect: CrIS overpasses occur at 13:30 LT, close to the daily peak in NH_3 concentrations, and while LOTOS-EUROS simulates the diurnal cycle and model equivalents are sampled at the overpass time, the model may underestimate the amplitude of the daytime peak, contributing to the systematic offset. By contrast, IASI overpasses at 09:30 LT do not coincide with a concentration extremum, which is consistent with the considerably better agreement between retrieved and simulated IASI columns (Fig. 7c,d). Winter months (December–January) show considerable spatial noise in the CrIS retrievals, consistent with reduced thermal contrast and increased cloud contamination.

For IASI (Fig. 7c,d), the comparison is reversed: the model simulations are generally higher than the IASI retrievals, suggesting a possible low bias in the IASI product or a regional overestimation in the model for certain months. The IASI retrievals are considerably more spatially scattered than CrIS, particularly in winter, where the sparse and noisy retrieval coverage makes robust comparison difficult. Despite these instrument-specific biases, the overall spatial and temporal structures of both retrievals are broadly consistent with each other and with the model, lending confidence to the assimilation framework. The opposing sign of the model bias between the two instruments may partly reflect differences in their averaging kernel conventions (Sect. 2.2), and is noted as a source of structural uncertainty in the joint assimilation.

Figure 6(b) presents the posterior scaling factors derived from the joint assimilation of real CrIS and IASI satellite observations, with results for each individual instrument provided in the Supplement. The satellite inversion produces substantial upward adjustments to the prior emission inventory throughout most of the year, with the exception of March and April, where the posterior scaling factors show downward corrections. This reversal likely reflects the fact that the prior emission time profile prescribes its strongest emissions during spring, bringing the model into closer agreement with observations in these months and allowing the inversion to detect a relative overestimation in the prior during this period.

A likely contributor to these large upward adjustments is the single-peak emission time profile prescribed in the prior, as discussed above. Observed ammonia concentrations exhibit a secondary summer peak (Fig. A1b and Fig. S16), which the prior does not capture. A similar secondary summer signal is also visible in the satellite total column retrievals (Fig. 7), suggesting that the summer elevation is not an artefact of the ground-based network but reflects a broader atmospheric signal. It is worth

https://doi.org/10.5194/egusphere-2026-4245
Preprint. Discussion started: 10 August 2026

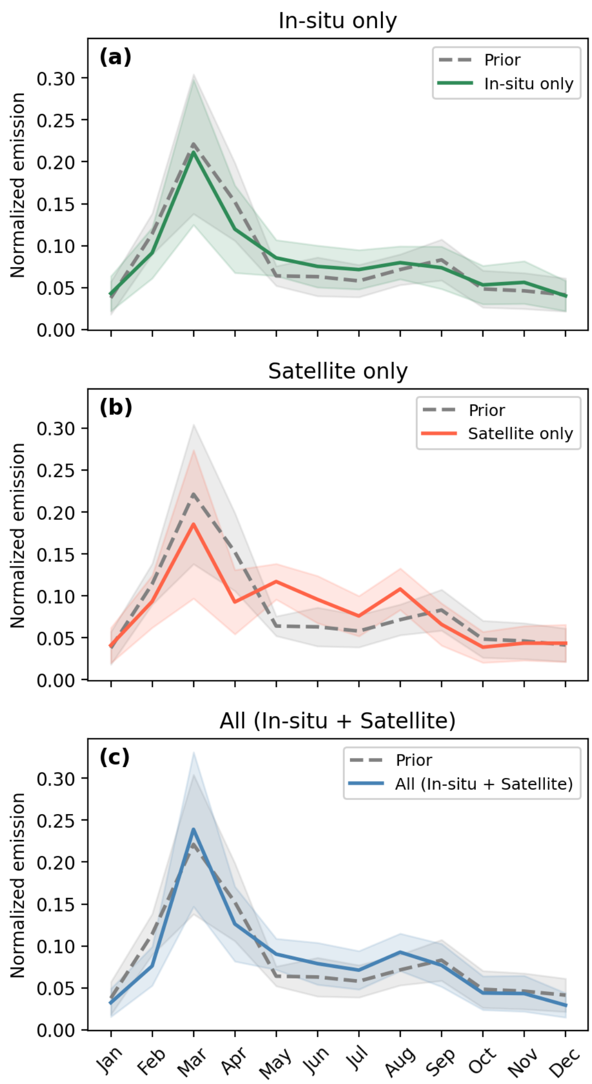

Figure 8. Seasonal NH_3 emission time profiles for the prior (dashed grey) and posterior under three assimilation configurations, spatially normalised relative to the annual domain mean. Shaded areas indicate spatial variability ($\pm 1\sigma$) across grid cells.

noting that 2022 showed an unusually strong spring peak in March, whereas April is typically the dominant spring month in other years, which may influence the posterior adjustments during this period.

The satellite-derived posterior adjustments during summer therefore likely reflect a combination of two factors: a genuine underestimation of NH_3 source strength in the prior inventory during summer months, and a temporal misallocation in the prescribed emission time profile. Disentangling these two contributions requires either an updated prior time profile or independent validation against measurements not used in the assimilation.

https://doi.org/10.5194/egusphere-2026-4245
Preprint. Discussion started: 10 August 2026

3.2.3 Results with combined in situ and satellite observations

Figure 6(c) shows the posterior scaling factors derived from the joint assimilation of real in situ and satellite observations. Prior to the inversion, normalisation was applied to account for differences in units and magnitude between the two data streams. The combined result broadly resembles a weighted blend of the satellite-only and in situ-only posteriors: spring months (March and April) show downward adjustments to the scaling factor, while summer months show upward corrections. Importantly, the magnitude of these adjustments is considerably more moderate than in the satellite-only case, consistent with the earlier finding that joint assimilation reduces the influence of spurious satellite-driven signals.

The coastal–inland contrast identified in the in situ results persists in the combined inversion, manifesting in two distinct modes: in May through August, the pattern is largely one-sided, with coastal areas showing emission increases while inland regions remain closer to the prior; in September, October, and December, more spatially heterogeneous changes emerge, with both positive and negative adjustments across the domain. Furthermore, months that align more closely with the in situ results, such as February, October, November, and December, correspond to periods of reduced satellite retrieval availability due to cloud cover and precipitation characteristic of Dutch weather conditions. This suggests that in situ observations effectively fill the observational gap during retrieval-poor months; February in particular demonstrates that combining in situ with satellite data can provide meaningful emission constraints even under conditions of limited satellite coverage.

Figure 6(d) presents the posterior emission rates derived from the combined assimilation. Despite the apparent magnitude of changes in the scaling factors, the posterior emission field shows a relatively stable spatial structure throughout the year, with emissions peaking in March consistent with the spring manure application season, and summer months showing moderate increases that do not reach the spring maximum. Figure 8 further characterises the posterior temporal structure by presenting domain-averaged normalised seasonal emission profiles for all three assimilation configurations. All configurations broadly preserve the prior seasonal structure, with peak emissions in spring and a gradual decline through summer and autumn, confirming that the inversion adjusts primarily the overall emission magnitude rather than the temporal allocation, consistent with the monthly-mean inversion framework applied here. Notable differences emerge between configurations. The satellite-only posterior suggests a relative reduction in spring emissions compared to the prior, alongside a more pronounced elevation during summer months, consistent with the large upward scaling factors identified in Fig. 6(b) and the known underrepresentation of the secondary summer NH_3 peak in the prior time profile. The in situ-only posterior shows comparatively small deviations from the prior throughout the year, which may partly reflect the deployment of MAN stations in nature conservation areas away from primary emission sources, limiting their sensitivity to seasonal emission variability at the source level (see Sect. 3.3). The combined posterior occupies an intermediate position, moderating the satellite-driven summer increase while retaining a modest seasonal adjustment signal, suggesting that the joint assimilation effectively balances the complementary strengths and biases of the two observation streams.

Figure 9 provides an annual mean overview of the prior and posterior NH_3 emissions and concentrations across all three assimilation configurations. In the emission field (a), the satellite-only posterior shows pronounced upward adjustments relative to the prior, particularly over the major agricultural regions including Friesland, the Gelderse Vallei (Food Valley), Noord-

https://doi.org/10.5194/egusphere-2026-4245
Preprint. Discussion started: 10 August 2026

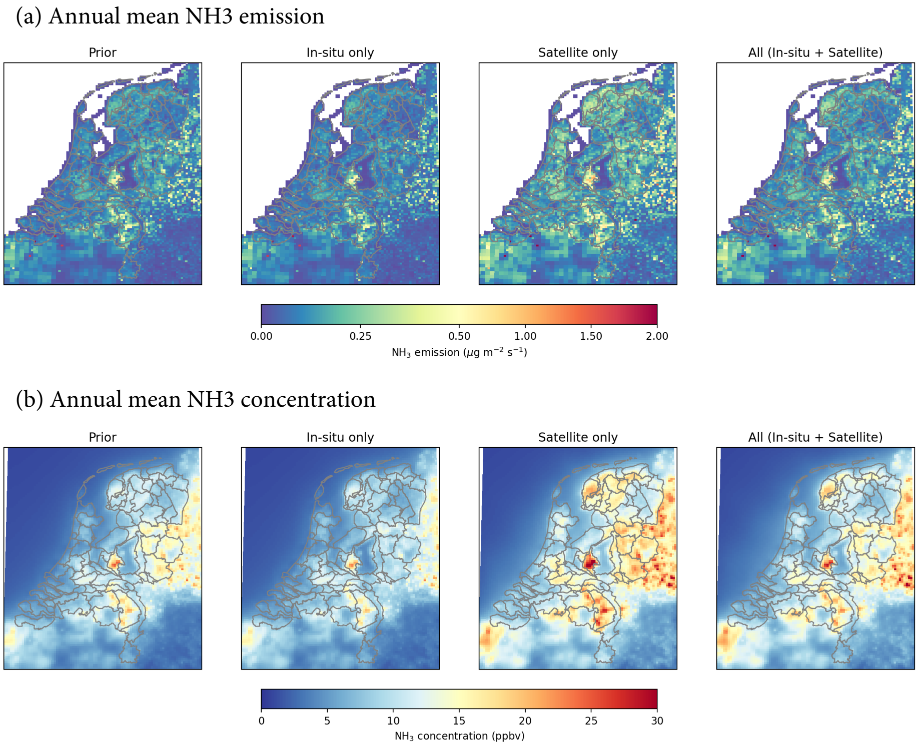

Figure 9. Annual mean NH_3 emission (a) and assimilated concentration (b) for the prior and three posterior configurations: in situ only (MAN+LML), satellite only (CrIS+IASI), and combined in situ and satellite. Emissions and concentrations are derived from the posterior ensemble mean of the LEKF system, averaged across all months of 2022.

Brabant, and eastern Netherlands, as well as across the Belgian and German border regions. The in situ-only posterior, by contrast, produces downward adjustments in eastern Netherlands, where ground-based observations suggest the prior inventory overestimates emissions in this region. The combined posterior lies between these two extremes, moderating the large satellite-driven upward corrections while partially preserving the downward signal detected by the in situ network.

These contrasting adjustments are reflected in the annual mean concentration fields (b). The satellite-only posterior produces substantially elevated NH_3 concentrations across the agricultural core of the Netherlands, with localised hotspots exceeding 30 ppbv in the Gelderse Vallei (Food Valley) and Noord-Brabant regions. The in situ-only posterior remains close to the prior concentration field. The combined posterior shows intermediate concentrations, with elevated values in the agriculturally intensive regions that are less extreme than the satellite-only case, reflecting the stabilising role of ground-based observations in the joint assimilation.

https://doi.org/10.5194/egusphere-2026-4245
Preprint. Discussion started: 10 August 2026

3.3 Discussion

3.3.1 System performance and limiting factors

The synthetic and real-data results together reveal three recurring limitations that govern the performance of the LEKF inversion system across all observation configurations:

(1) The regularisation parameter γ is necessary to prevent overfitting given the large number of gridded satellite observations, but it systematically dampens the magnitude of the posterior adjustment that the inversion can resolve. This explains why posterior scaling factors consistently remain closer to the prior than the true perturbation values in the synthetic experiments.

(2) The isotropic localisation radius of 15 km does not account for the directional character of NH_3 plume transport: in reality, instantaneous NH_3 transport is directional, with the observational footprint of a given station elongated in the prevailing wind direction at any given time, as mentioned in Sect. 3.1.1. A flow-dependent localisation scheme that accounts for the climatological wind field could better represent these advective relationships at the monthly timescale and is identified as a direction for future development.

(3) The single-peak prior emission time profile on monthly basis, which does not capture the observed secondary summer concentration peak, introduces a systematic bias into both the in situ and satellite inversions during summer months; correcting this would require either an updated prior time allocation or an inversion framework that simultaneously optimises both emission magnitudes and their temporal distribution.

A further contributor to the systematic upward adjustments in the satellite-only inversion may be the diurnal sampling bias inherent to polar-orbiting instruments: both CrIS and IASI acquire retrievals during daytime overpasses, when boundary-layer NH_3 concentrations may differ from the daily mean. Although the application of satellite averaging kernels within the observation operator accounts for vertical sensitivity differences between the retrieval and the model, the diurnal cycle of NH_3 concentrations simulated by LOTOS-EUROS remains uncertain. If the model underestimates daytime NH_3 concentrations relative to the true atmospheric state, the daytime-biased satellite observations may systematically exceed the model equivalent, driving spurious upward corrections to the emission inventory that are not representative of the true 24-hour emission budget.

Hourly LML concentration measurements provide some insight into the diurnal NH_3 cycle, though surface concentration measurements do not fully represent the diurnal variability of the total column density, particularly given the spatiotemporal heterogeneity in the vertical distribution of NH_3 (Clarisse et al., 2021; Zeng et al., 2023). A more systematic analysis of the diurnal emission profile and its implications for satellite sampling bias is identified as a direction for future work. In this context, the availability of nighttime IASI overpasses (21:30 LT) alongside the daytime retrievals used in this study offers a direct opportunity to quantify the diurnal sampling bias by comparing daytime and nighttime column retrievals over the same domain, without requiring additional ground-based measurements.

As discussed in Sect. 2.4.1, decomposing MAN observations into the monthly climatology, network-wide spatial mean, and residual local anomalies reveals a significant limitation: the local anomalies remaining after signal removal are characterised by large random variability and weak spatial structure, suggesting that MAN observations carry limited information about fine-scale emission gradients at the sub-provincial level.

https://doi.org/10.5194/egusphere-2026-4245
Preprint. Discussion started: 10 August 2026

This limitation is compounded by the deployment strategy of the MAN network, which was designed to monitor ambient NH_3 concentrations in nature conservation areas rather than to characterise agricultural emission sources. As a result, MAN stations are systematically located away from the dominant NH_3 emission sources, and given the short atmospheric lifetime of ammonia and its reactivity, concentrations measured at MAN sites primarily reflect background and regionally transported NH_3 rather than direct source signals. In this sense, the MAN network functions as a regional background monitor, providing a spatially coherent reference against which domain-scale emission changes can be detected, rather than as a proximal emission monitoring system capable of resolving local source heterogeneity.

This distinction has direct implications for the inversion results presented here. The in situ-only posterior (Fig. 6a) reflects the aggregate constraint of a background-sensitive network: it captures domain-scale and seasonal emission signals reasonably well but cannot resolve the sub-provincial patterns that drive the largest uncertainties in the Dutch NH_3 budget. Improving sub-provincial constraints would require higher-temporal-resolution or measurements closer to emission sources.

The synthetic perturbation experiments presented in Sect. 3.1 serve as the primary evaluation framework for the LEKF system, providing a controlled assessment of the inversion performance under known emission perturbations. In the real-data application, however, a fundamental limitation arises: since all available observations are assimilated to maximise the emission constraint, no independent observations remain for out-of-sample validation of the posterior estimates. The posterior emission fields are therefore evaluated indirectly through their physical consistency — the recovery of known seasonal patterns and the chi-square diagnostic criterion — rather than through direct comparison with withheld measurements. Future work should consider a leave-one-out or split-network validation strategy, in which a subset of observations is withheld from the assimilation and used to independently evaluate the posterior concentration fields.

3.3.2 Observation effectiveness and network optimisation

The observation effectiveness quantifies the relative contribution of each observation to the posterior state update and is defined in Sect. 2.4.4 (Eq. 8); see also Li et al. (2025). Figure A2 shows the maximum observation effectiveness across all months for each in situ station. Stations with lower peak effectiveness (red) do not necessarily fail to constrain emissions; their influence may be distributed across multiple months or shared among neighbouring stations within the localisation radius.

Figure 10 presents the domain-wide observation effectiveness derived from the synthetic inversion, with a hypothetical measurement site assigned to every model grid cell (approximately every 4 km). The spatial pattern of high effectiveness values broadly coincides with the major agricultural emission source regions, most notably the Gelderse Vallei (Food Valley) in the centre-east and Noord-Brabant in the south. This alignment suggests that additional monitoring in these areas would most effectively constrain high-intensity NH_3 emission estimates.

Notably, these high-effectiveness regions correspond to areas where both the MAN and LML networks have limited coverage. As discussed above, MAN stations are deliberately sited in nature conservation areas. Unexpectedly, LML coverage in these high-sensitivity regions is also limited, despite the network not being subject to the same nature-area deployment constraints as MAN. This mismatch between emission optimal monitoring locations and current station deployment reinforces the conclusion that the existing ground-based networks provide background-level constraints rather than proximal emission

https://doi.org/10.5194/egusphere-2026-4245
Preprint. Discussion started: 10 August 2026

monitoring, and highlights where targeted expansion would be most beneficial for improving sub-provincial NH_3 emission quantification.

The results should be interpreted as qualitative guidance rather than a prescriptive optimisation. As discussed in Li et al. (2025), concentrating a large number of "high-quality" measurements in a single region can shift the system from a measurement-limited to a model-limited regime, in which the posterior is increasingly constrained by model structural errors rather than observational information. The domain-wide effectiveness map therefore indicates priority regions for network expansion, while the practical deployment of additional stations would require careful consideration of the trade-off between spatial coverage and observational redundancy within the localisation.

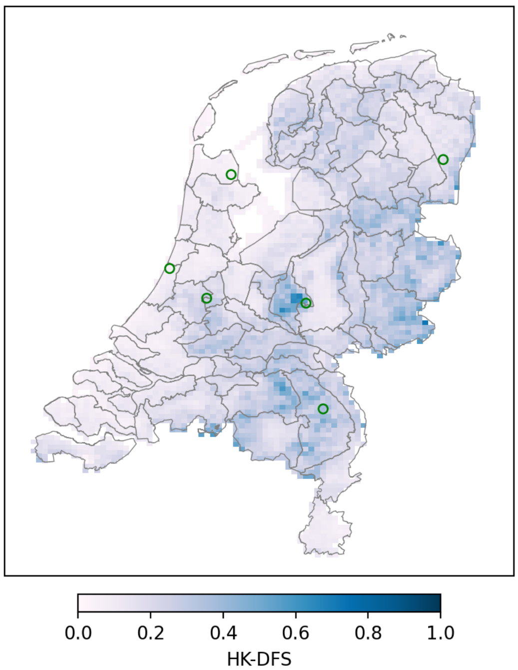

Figure 10. Observation effectiveness across all months for each model grid cell, derived from the synthetic inversion assuming a hypothetical measurement site at every grid cell location. Higher values indicate grid cells where an additional observation would most strongly constrain the posterior NH_3 emission estimate. The green circles denote the existing LML sites.

4 Conclusion and future work

This study presents an offline localized ensemble Kalman filter (LEKF) system coupled with the LOTOS-EUROS chemical transport model for the inversion of monthly NH_3 emissions over the Netherlands using observations in 2022. The system was evaluated through synthetic perturbation experiments before being applied to real observations from in situ networks (MAN+LML) and satellite instruments (CrIS+IASI).

https://doi.org/10.5194/egusphere-2026-4245
Preprint. Discussion started: 10 August 2026

Summary of findings

The synthetic experiments demonstrate that the system's performance depends strongly on both the spatial structure of the emission perturbation and the observation configuration. Under domain-wide uniform reduction scenarios, all observation configurations reliably detect the imposed emission trend, though posterior scaling factors consistently remain above the true value, reflecting the dampening effect of regularisation. For spatially heterogeneous perturbations, performance degrades substantially across all configurations: atmospheric transport disperses localised concentration signals before they reach observation locations; satellite column retrievals modulated by the averaging kernel are insensitive to fine-scale near-surface gradients; and the regularisation required to stabilise the overdetermined system suppresses small-amplitude spatial variations.

The progressive addition of observation types reveals a consistent hierarchy of constraint strength. In situ observations (MAN+LML) provide spatially sharp but geographically limited constraints, effectively recovering emission patterns in the vicinity of station clusters while leaving unmonitored regions poorly constrained. Satellite observations (CrIS+IASI) provide broad spatial coverage but produce smoother posterior fields and tend to drive systematic upward adjustments to the prior inventory, particularly during summer months. These adjustments are at least partly attributable to the monotonic prior emission time profile, which does not capture the observed secondary summer NH_3 concentration peak and may therefore cause the satellite observations to systematically exceed the model equivalent during this period. Combining both data streams moderates the satellite-driven upward adjustments and fills observational gaps during relatively retrieval-poor winter months, demonstrating the complementary value of the two observation types.

An important caveat concerns whether NH_3 concentration measurements alone are sufficient to constrain emissions. The inversion system optimises emission scaling factors by minimising the mismatch between modelled and observed NH_3 concentrations; however, concentration observations integrate the effects of emissions, atmospheric transport, chemistry, and deposition. Systematic errors in any of these processes can be absorbed into the posterior emission estimate, potentially leading to physically implausible adjustments. The large upward corrections produced by the satellite-only inversion during summer months illustrate this risk: while the posterior satisfies the observational constraint, the signal is likely partly driven by model structural errors rather than true emission underestimation.

Applied to real observations, the inversion yields emission estimates that reveal systematic regional adjustments relative to the prior inventory, particularly in agriculturally intensive areas during spring. The recovered seasonal patterns, elevated spring emissions during manure application, suppressed winter emissions, are physically consistent with known NH_3 volatilisation dynamics.

Limitations and future directions

Several limitations identified in this study point toward productive directions for future development. The isotropic 15 km localisation radius does not account for the directional character of NH_3 plume transport; wind-aware anisotropic localisation, which aligns the localisation kernel with the local wind field, is a natural next step and is currently under development. The monotonic prior emission time profile introduces systematic biases in summer months and should be replaced with a time allocation that reflects the observed bimodal seasonal cycle of NH_3 concentrations. The treatment of transboundary emission contributions as fixed boundary conditions means that errors in neighbouring-country inventories propagate into the Dutch posterior as unresolved systematic biases; future work should assess the sensitivity of the inversion to these transboundary uncertainties.

Also, the current study is limited to a single year (2022), which constrains the robustness of the posterior emission estimates and precludes trend analysis. Extending the inversion to multiple years would provide more statistically representative emission estimates and enable the detection of interannual variability and long-term trends in Dutch NH_3 emissions. However, the computational cost of running the LEKF system over extended periods remains a practical limitation with the current implementation.

A promising direction to address this is the use of machine learning to emulate the ensemble simulations required by the Kalman filter, substantially reducing the computational burden. Sitwell (2026) demonstrated that an AI-based ensemble emulator can reproduce atmospheric chemical ensemble behaviour at a fraction of the computational cost (reported to be over three orders of magnitude faster) of conventional model runs, making multi-year or near-real-time inversions tractable. A complementary effort is already underway within our group, where a deep learning emulator trained on LOTOS-EUROS simulations (Pang et al., 2026) has demonstrated high predictive accuracy for atmospheric pollutant concentration fields. Coupling this emulator with the LEKF system represents a natural next step, with the longer-term goal of enabling computationally efficient multi-year emission inversions and ultimately operational NH_3 emission monitoring over the Netherlands.

Finally, the observational landscape for NH_3 remote sensing is set to expand significantly in the coming years. The next-generation IASI-NG instrument, to be launched aboard the MetOp-SG satellites, will provide substantially improved spectral resolution and retrieval sensitivity compared to the current IASI product. More transformatively, the Infrared Sounder (IRS) aboard the upcoming Meteosat Third Generation (MTG) geostationary platform will enable continuous daytime NH_3 monitoring at high temporal resolution, overcoming the diurnal sampling limitations of polar-orbiting instruments identified in this study. Incorporating these next-generation observations into the LEKF framework represents a major opportunity to improve both the temporal resolution and the accuracy of NH_3 emission inversions over Europe.

Code and data availability. The LOTOS-EUROS is an open-sourced model, and the version v2.3 used for the study can be found on the official TNO website (https://airqualitymodeling.tno.nl/lotos-euros/open-source-version/, last access: 13 May 2026). The Measuring Ammonia in Nature (MAN) can be accessed through MAN website (https://man.rivm.nl/, last access: 13 November 2025). For LML measurement: https://www.luchtmeetnet.nl/ (last access: 13 November 2025). The satellite products CrIS and IASI are available from CrIS Fast Physical Retrieval Ammonia Database (https://hpfx.collab.science.gc.ca/~mas001/satellite_ext/cris/, last access: 13 November 2025) and IASI Portal (https://iasi.aeris-data.fr/nh3/, last access: 13 November 2025), respectively. The shapefile of Panorama Landschap is provided in https://www.nationaalgeoregister.nl/geonetwork/srv/api/records/fbf78109-07e2-47aa-afe6-6ab813f3d4f7?language=all, last access: 13 May 2026.

https://doi.org/10.5194/egusphere-2026-4245
Preprint. Discussion started: 10 August 2026

Appendix A: Ensemble Kalman Filter Formulation with Localisation

This appendix provides the mathematical derivation of the localized ensemble Kalman filter implementation used in this study.

The ensemble mean and perturbation matrix are defined as:

$$\bar{\boldsymbol{x}} = \frac{1}{m}\sum_{i=1}^{m}\boldsymbol{x}_i \tag{A1}$$

$$\mathbf{X} = [\boldsymbol{x}_1 - \bar{\boldsymbol{x}}, \ldots, \boldsymbol{x}_m - \bar{\boldsymbol{x}}] \tag{A2}$$

where m is the ensemble size and $\boldsymbol{x}_i$ represents the i-th ensemble member. The observation-space perturbation matrix is obtained by applying the observation operator:

$$\mathbf{Y} = \mathbf{H}\mathbf{X} \tag{A3}$$

The forecast error covariance is computed from the ensemble as:

$$\mathbf{P}^f = \frac{1}{m-1}\sum_{i=1}^{m}(\boldsymbol{x}_i - \bar{\boldsymbol{x}})(\boldsymbol{x}_i - \bar{\boldsymbol{x}})^T = \frac{1}{m-1}\mathbf{X}\mathbf{X}^T \tag{A4}$$

To avoid explicit computation of $\mathbf{P}^f$, we define the square-root covariance matrix $\mathbf{S}$, such that:

$$\mathbf{P}^f = \mathbf{S}\mathbf{S}^T \tag{A5}$$

$$\mathbf{S} = \frac{1}{\sqrt{m-1}}[\boldsymbol{x}_1 - \bar{\boldsymbol{x}}, \ldots, \boldsymbol{x}_m - \bar{\boldsymbol{x}}] = \frac{1}{\sqrt{m-1}}\mathbf{X} \tag{A6}$$

Correspondingly, the observation-space square-root covariance is:

$$\boldsymbol{\Psi} = \mathbf{H}\mathbf{S} = \frac{1}{\sqrt{m-1}}\mathbf{Y} \tag{A7}$$

The Kalman gain can be reformulated using the square-root matrices:

$$\begin{aligned}\mathbf{K} &= \mathbf{P}^f\mathbf{H}^T\left[\mathbf{H}\mathbf{P}^f\mathbf{H}^T + \mathbf{R}\right]^{-1}\\ &= \mathbf{S}\mathbf{S}^T\mathbf{H}^T\left[\mathbf{H}\mathbf{S}\mathbf{S}^T\mathbf{H}^T + \mathbf{R}\right]^{-1}\\ &= \mathbf{S}\boldsymbol{\Psi}^T\left[\boldsymbol{\Psi}\boldsymbol{\Psi}^T + \mathbf{R}\right]^{-1}\end{aligned} \tag{A8}$$

This formulation avoids explicit computation of the $(n \times n)$ matrix $\mathbf{P}^f$ by working with the $(n \times m)$ matrix $\mathbf{S}$ and the $(p \times m)$ matrix $\boldsymbol{\Psi}$, where n is the state dimension and p is the observation dimension.

To mitigate spurious long-range correlations arising from finite ensemble size, we apply covariance localisation through the element-wise (Hadamard) multiplication. The innovation covariance with localisation is:

$$\boldsymbol{\Gamma} = \left(\boldsymbol{\Psi}\boldsymbol{\Psi}^T\right) \odot \mathbf{L}^o + \mathbf{R} \tag{A9}$$

https://doi.org/10.5194/egusphere-2026-4245
Preprint. Discussion started: 10 August 2026

where $\mathbf{L}^o$ is the localisation matrix in observation space and $\odot$ denotes Hadamard multiplication. The localisation matrix elements are computed using a Gaussian correlation function with compact support:

$$L_{ij}^o = \begin{cases} \exp\left(-\frac{1}{2}\left(\frac{d_{ij}}{\rho}\right)^2\right) & \text{if } d_{ij} \le c \cdot \rho \\ 0 & \text{if } d_{ij} > c \cdot \rho \end{cases} \tag{A10}$$

where d_{ij} is the distance between observation locations i and j, ρ is the localisation length scale (set to 15 km in this study, detailed analysis shown in Sect. 2.4.1 and Fig. A1), and $c = 3.5$ is a cutoff factor beyond which correlations are set to zero for computational efficiency.

The Kalman gain is computed by solving the linear system via Cholesky decomposition. Let $\mathbf{\Gamma} = \mathbf{\Lambda}\mathbf{\Lambda}^T$ where $\mathbf{\Lambda}$ is lower triangular. The Kalman gain satisfies:

$$\mathbf{\Lambda}\mathbf{\Lambda}^T\mathbf{K}^T = \mathbf{\Psi}\mathbf{S}^T \tag{A11}$$

This system is solved efficiently through forward and backward substitution without explicitly computing the inverse of $\mathbf{\Gamma}$. The analysis ensemble members are then updated:

$$\boldsymbol{x}_i^a = \boldsymbol{x}_i^f + (\mathbf{K} \odot \mathbf{L})\left(\boldsymbol{y}^o - \mathbf{H}\boldsymbol{x}_i^f + \boldsymbol{v}_i\right) \tag{A12}$$

where $\mathbf{L}$ is the state-space localisation matrix and $\boldsymbol{v}_i \sim \mathcal{N}(\mathbf{0}, \mathbf{R})$ represents perturbed observation errors to maintain ensemble spread.

Following Eqs. (7) and (A12), the averaging kernel is derived from the forecast and posterior error covariance matrices, where $\mathbf{P}^a$ is estimated from the posterior ensemble as:

$$\begin{aligned} \mathbf{P}^a &= \frac{1}{m-1}\sum_{i=1}^{m}\left(\boldsymbol{x}_i^a - \bar{\boldsymbol{x}}^a\right)\left(\boldsymbol{x}_i^a - \bar{\boldsymbol{x}}^a\right)^T \\ &= \frac{1}{m-1}\mathbf{X}^a\mathbf{X}^{aT} \end{aligned} \tag{A13}$$

where $\bar{\boldsymbol{x}}^a$ is the posterior ensemble mean, and $\mathbf{X}^a$ is the matrix of posterior ensemble perturbations.

The observation effectiveness HK-DFS, discussed and defined in Sect. 2.4.4, is computed through the term $\mathbf{HK}$. Using the square-root formulation, it can be expressed as:

$$\begin{aligned} \mathbf{HK} &= \mathbf{HS}\mathbf{\Psi}^T\left[\mathbf{\Psi}\mathbf{\Psi}^T + \mathbf{R}\right]^{-1} \\ &= \mathbf{\Psi}\mathbf{\Psi}^T\left[\mathbf{\Psi}\mathbf{\Psi}^T + \mathbf{R}\right]^{-1} \end{aligned} \tag{A14}$$

This can be computed efficiently by solving:

$$\mathbf{\Lambda}\mathbf{\Lambda}^T(\mathbf{HK})^T = \mathbf{\Psi}\mathbf{\Psi}^T \tag{A15}$$

using the same Cholesky factor $\mathbf{\Lambda}$ from the Kalman gain computation, thereby avoiding redundant matrix factorisations. An example of the observation effectiveness is shown in Fig. A2.

https://doi.org/10.5194/egusphere-2026-4245
Preprint. Discussion started: 10 August 2026

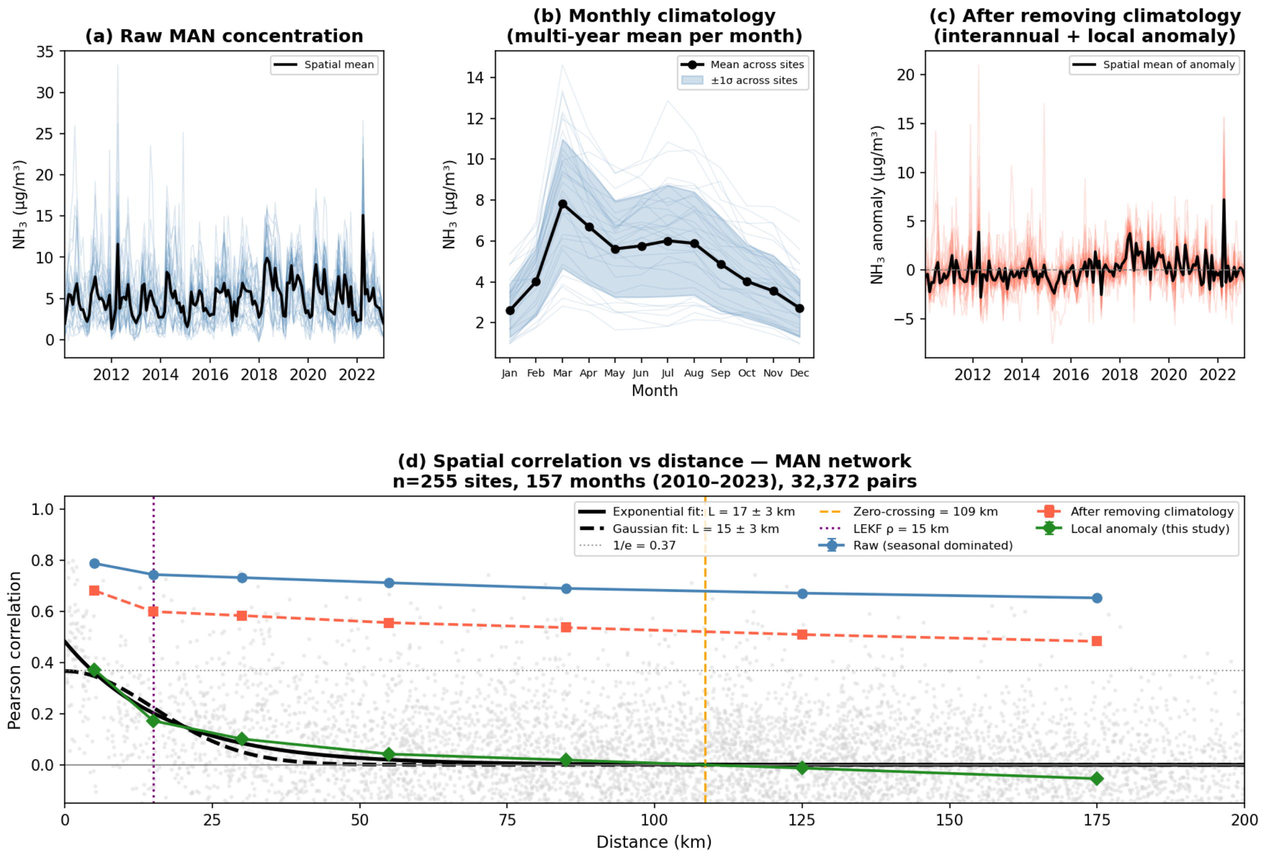

Figure A1. Spatial correlation length analysis of the MAN (Measuring Ammonia in Nature) ground-based NH_3 monitoring network (255 sites, 2010–2023). **(a)** Measured monthly NH_3 concentrations showing strong seasonal variability common to all sites. **(b)** Multi-year monthly climatology (mean $\pm$ 1σ across sites), illustrating the dominant seasonal cycle (winter minimum, spring/summer maximum) that drives inter-site correlations. **(c)** Anomalies after removing the monthly climatology, retaining interannual variability and local spatial structure. **(d)** Binned spatial correlation as a function of inter-site distance for each processing stage. Measured concentrations (blue) and climatology-removed anomalies (red) exhibit correlations well above $1/e$ throughout the Netherlands domain (~300 km), reflecting the dominance of seasonal and interannual common signals rather than true spatial structure. Local anomalies (green), after removing both the climatological and interannual common signals, decay rapidly with distance and cross zero at ~107 km. Fitted exponential and Gaussian decay functions yield correlation lengths of $\rho = 17 \pm 3$ km and $\rho = 15 \pm 3$ km, respectively, consistent with the localisation radius ($\rho = 15$ km, purple dotted line) used in the LEKF system and with the spatial scale of NH_3 point-source plumes (~3–7 km grid scale).

https://doi.org/10.5194/egusphere-2026-4245
Preprint. Discussion started: 10 August 2026

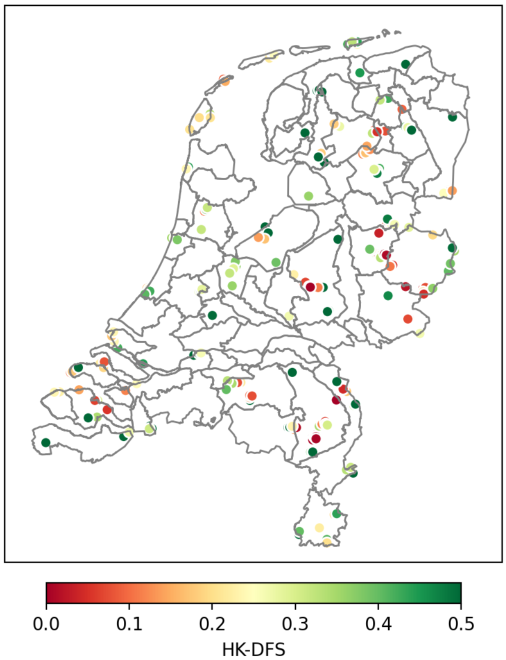

Figure A2. Maximum observation effectiveness across all months for each in situ station, derived from the real MAN+LML inversion. Green colours indicate higher peak effectiveness (stronger influence on the posterior state), while red colours indicate lower peak effectiveness.

Appendix B: Optimisation of α

In this study, a combined error is applied to the inversion with residual and measurement errors to construct the total observational error (see Eq. 5), where:

- $\varepsilon_{\text{residual}} = (\boldsymbol{z} - \overline{\boldsymbol{z}})$ is the residual error vector, representing the spread in observation-minus-model misfits across ensemble members;
- $\boldsymbol{z} = \boldsymbol{y}^o - \mathbf{H}\boldsymbol{x}$ denotes the innovation (misfit between observations and forward model simulations);
- α is a scaling factor to optimised through χ^2 testing;
- $\varepsilon_{\text{measurement}}$ is the measurement error. For MAN, $\varepsilon_{\text{MAN}} = \sqrt{0.90^2 + (0.28 \times \boldsymbol{c})^2}$ (in μg m^{-3}, Lolkema et al., 2015; Noordijk et al., 2020); for satellite data, it is the retrieval error provided in the product; for LML, the measurement error is 1% (Berkhout et al., 2017).

Following Li et al. (2025), we define a performance score s_{χ^2} to evaluate both statistical consistency (p-value) and goodness-of-fit (normalized chi-square, NCS):

$$s_{\chi^2} = p \cdot e^{-|1-\text{NCS}|}, \tag{B1}$$

where:

- p is the p-value from the χ^2 test, with higher values indicating better statistical consistency;
- $\text{NCS} = \dfrac{\boldsymbol{z}^T\mathbf{R}^{-1}\boldsymbol{z}}{\text{DOF}}$ is the normalized chi-square statistic, which should approach 1 for optimally characterized errors;
- DOF (degrees of freedom) represents the number of independent observational constraints;
- $\mathbf{R}$ is the observational error covaraince.

The optimal α maximizes s_{χ^2}, balancing statistical consistency with appropriate fit quality.

Author contributions. SL: methodology, software, formal analysis, writing (original draft), visualisation. ED: conceptualisation, software, writing (review and editing), supervision, project administration, funding acquisition. BHG: software, methodology, writing (review and editing). AS: software, methodology, writing (review and editing). MWS: data, methodology, writing (review and editing). SvdG: data, methodology, writing (review and editing). RWK: data, methodology, writing (review and editing). MVD: data, methodology, writing (review and editing). LC: data, methodology, writing (review and editing). JWE: conceptualisation, validation, writing (review and editing), supervision, project administration, funding acquisition.

Competing interests. The authors declare that no competing interests are present.

Acknowledgements. This study was funded by the Dutch Ministry of Agriculture, Nature and Food Quality (LNV), within the framework of the National Nitrogen Knowledge Programme (NKS), project NKS-SAGEN, on satellite observations and ensemble modeling. M. Van Damme is grateful for the FED-TWIN ARENBERG grant. Research activities in Belgium are also funded through the HIRS and BEAM projects supported by BELSPO. L. Clarisse is Senior Research Associate supported by the Belgian F.R.S.-FNRS. We also acknowledge the use of Claude (claude.ai) to assist in refining the language used in this document.

References

Berkhout, A. J. C., Swart, D. P. J., Volten, H., Gast, L. F. L., Haaima, M., Verboom, H., Stefess, G., Hafkenscheid, T., and Hoogerbrugge, R.: Replacing the AMOR with the miniDOAS in the ammonia monitoring network in the Netherlands, Atmospheric Measurement Techniques, 10, 4099–4120, https://doi.org/10.5194/amt-10-4099-2017, 2017.

Chen, M., Zhang, W., Han, W., Xia, J., and Jin, J.: Global ammonia emission inversion in 2022 via assimilating IASI observations, npj Clean Air, 2, 35, https://doi.org/10.1038/s44407-026-00072-7, 2026.

Clarisse, L., Van Damme, M., Hurtmans, D., Franco, B., Clerbaux, C., and Coheur, P.-F.: The Diel Cycle of NH3 Observed From the FY-4A Geostationary Interferometric Infrared Sounder (GIIRS), Geophysical Research Letters, 48, e2021GL093 010, https://doi.org/10.1029/2021GL093010, 2021.

Clarisse, L., Franco, B., Van Damme, M., Di Gioacchino, T., Hadji-Lazaro, J., Whitburn, S., Noppen, L., Hurtmans, D., Clerbaux, C., and Coheur, P.: The IASI NH_3 version 4 product: averaging kernels and improved consistency, Atmospheric Measurement Techniques, 16, 5009–5028, https://doi.org/10.5194/amt-16-5009-2023, 2023.

Clerbaux, C., Boynard, A., Clarisse, L., George, M., Hadji-Lazaro, J., Herbin, H., Hurtmans, D., Pommier, M., Razavi, A., Turquety, S., Wespes, C., and Coheur, P.-F.: Monitoring of atmospheric composition using the thermal infrared IASI/MetOp sounder, Atmospheric Chemistry and Physics, 9, 6041–6054, https://doi.org/10.5194/acp-9-6041-2009, 2009.

Dammers, E., McLinden, C. A., Griffin, D., Shephard, M. W., Van Der Graaf, S., Lutsch, E., Schaap, M., Gainairu-Matz, Y., Fioletov, V., Van Damme, M., Whitburn, S., Clarisse, L., Cady-Pereira, K., Clerbaux, C., Coheur, P. F., and Erisman, J. W.: NH_3 emissions from large point sources derived from CrIS and IASI satellite observations, Atmospheric Chemistry and Physics, 19, 12 261–12 293, https://doi.org/10.5194/acp-19-12261-2019, 2019.

Ding, J., van der A, R., Eskes, H., Dammers, E., Shephard, M., Wichink Kruit, R., Guevara, M., and Tarrason, L.: Ammonia emission estimates using CrIS satellite observations over Europe, Atmospheric Chemistry and Physics, 24, 10 583–10 599, https://doi.org/10.5194/acp-24-10583-2024, 2024.

Erisman, J. W., Bleeker, A., Galloway, J., and Sutton, M. S.: Reduced nitrogen in ecology and the environment, Environmental pollution, 150, 140–149, https://doi.org/10.1016/j.envpol.2007.06.033, 2007.

Erisman, J. W., Sutton, M. A., Galloway, J., Klimont, Z., and Winiwarter, W.: How a century of ammonia synthesis changed the world, Nature Geoscience, 1, 636–639, https://doi.org/10.1038/ngeo325, 2008.

Erisman, J. W., Galloway, J. N., Seitzinger, S., Bleeker, A., Dise, N. B., Petrescu, A. M. R., Leach, A. M., and de Vries, W.: Consequences of human modification of the global nitrogen cycle, Philosophical Transactions of the Royal Society B: Biological Sciences, 368, https://doi.org/10.1098/rstb.2013.0116, 2013.

Evensen, G.: The Ensemble Kalman Filter: theoretical formulation and practical implementation, Ocean Dynamics, 53, 343–367, https://doi.org/10.1007/s10236-003-0036-9, 2003.

Ge, X., Schaap, M., and de Vries, W.: Improving spatial and temporal variation of ammonia emissions for the Netherlands using livestock housing information and a Sentinel-2-derived crop map, Atmospheric Environment: X, 17, 100 207, https://doi.org/10.1016/j.aeaoa.2023.100207, 2023.

Giannadaki, D., Giannakis, E., Pozzer, A., and Lelieveld, J.: Estimating health and economic benefits of reductions in air pollution from agriculture, Science of The Total Environment, 622-623, 1304–1316, https://doi.org/10.1016/j.scitotenv.2017.12.064, 2018.

https://doi.org/10.5194/egusphere-2026-4245
Preprint. Discussion started: 10 August 2026

Gu, B., Zhang, L., van Dingenen, R., Vieno, M., van Grinsven, H., Zhang, X., Zhang, S., Chen, Y., Wang, S., Ren, C., Rao, S., Holland, M., Winiwarter, W., Chen, D., Xu, J., and Sutton, M. A.: Abating ammonia is more cost-effective than nitrogen oxides for mitigating $PM_{2.5}$ air pollution, Science, 374, 758–762, https://doi.org/10.1126/science.abf8623, 2021.

Hersbach, H., Bell, B., Berrisford, P., Hirahara, S., Horányi, A., Muñoz Sabater, J., Nicolas, J., Peubey, C., Radu, R., Schepers, D., Simmons, A., Soci, C., Abdalla, S., Abellan, X., Balsamo, G., Bechtold, P., Biavati, G., Bidlot, J., Bonavita, M., De Chiara, G., Dahlgren, P., Dee, D., Diamantakis, M., Dragani, R., Flemming, J., Forbes, R., Fuentes, M., Geer, A., Haimberger, L., Healy, S., Hogan, R. J., Hólm, E., Janisková, M., Keeley, S., Laloyaux, P., Lopez, P., Lupu, C., Radnoti, G., de Rosnay, P., Rozum, I., Vamborg, F., Villaume, S., and Thépaut, J.-N.: The ERA5 global reanalysis, Quarterly Journal of the Royal Meteorological Society, 146, 1999–2049, https://doi.org/10.1002/qj.3803, 2020.

Kong, L., Tang, X., Zhu, J., Wang, Z., Pan, Y., Wu, H., Wu, L., Wu, Q., He, Y., Tian, S., Xie, Y., Liu, Z., Sui, W., Han, L., and Carmichael, G.: Improved Inversion of Monthly Ammonia Emissions in China Based on the Chinese Ammonia Monitoring Network and Ensemble Kalman Filter, Environmental Science & Technology, 53, 12 529–12 538, https://doi.org/10.1021/acs.est.9b02701, pMID: 31576752, 2019.

Kuenen, J., Dellaert, S., Visschedijk, A., Jalkanen, J.-P., Super, I., and Denier van der Gon, H.: CAMS-REG-v4: a state-of-the-art high-resolution European emission inventory for air quality modelling, Earth System Science Data, 14, 491–515, https://doi.org/10.5194/essd-14-491-2022, 2022.

Lelieveld, J., Evans, J. S., Fnais, M., Giannadaki, D., and Pozzer, A.: The contribution of outdoor air pollution sources to premature mortality on a global scale, Nature, 525, 367–371, https://doi.org/10.1038/nature15371, 2015.

Li, S., Dammers, E., Segers, A., and Erisman, J. W.: Local-scale inversion of agricultural ammonia emissions: a case study on Schiermonnikoog, the Netherlands, Atmospheric Chemistry and Physics, 25, 15 593–15 611, https://doi.org/10.5194/acp-25-15593-2025, 2025.

Lolkema, D. E., Noordijk, H., Stolk, A. P., Hoogerbrugge, R., van Zanten, M. C., and van Pul, W. A. J.: The Measuring Ammonia in Nature (MAN) network in the Netherlands, Biogeosciences, 12, 5133–5142, https://doi.org/10.5194/bg-12-5133-2015, 2015.

Lu, X., Jacob, D. J., Zhang, Y., Maasakkers, J. D., Sulprizio, M. P., Shen, L., Qu, Z., Scarpelli, T. R., Nesser, H., Yantosca, R. M., Sheng, J., Andrews, A., Parker, R. J., Boesch, H., Bloom, A. A., and Ma, S.: Global methane budget and trend, 2010–2017: complementarity of inverse analyses using in situ (GLOBALVIEWplus CH_4 ObsPack) and satellite (GOSAT) observations, Atmospheric Chemistry and Physics, 21, 4637–4657, https://doi.org/10.5194/acp-21-4637-2021, 2021.

Manders, A. M. M., Builtjes, P. J. H., Curier, L., Denier van der Gon, H. A. C., Hendriks, C., Jonkers, S., Kranenburg, R., Kuenen, J. J. P., Segers, A. J., Timmermans, R. M. A., Visschedijk, A. J. H., Wichink Kruit, R. J., van Pul, W. A. J., Sauter, F. J., van der Swaluw, E., Swart, D. P. J., Douros, J., Eskes, H., van Meijgaard, E., van Ulft, B., van Velthoven, P., Banzhaf, S., Mues, A. C., Stern, R., Fu, G., Lu, S., Heemink, A., van Velzen, N., and Schaap, M.: Curriculum vitae of the LOTOS-EUROS (v2.0) chemistry transport model, Geoscientific Model Development, 10, 4145–4173, https://doi.org/10.5194/gmd-10-4145-2017, 2017.

Manders-Groot, A. and LOTOS-EUROS team: LOTOS-EUROS v2.3.000 Reference Guide, https://airqualitymodeling.tno.nl/downloads/, 2023.

Noordijk, H., Braam, M., Rutledge-Jonker, S., Hoogerbrugge, R., Stolk, A., and van Pul, W.: Performance of the MAN ammonia monitoring network in the Netherlands, Atmospheric Environment, 228, 117 400, https://doi.org/10.1016/j.atmosenv.2020.117400, 2020.

Pai, S. J., Heald, C. L., and Murphy, J. G.: Exploring the Global Importance of Atmospheric Ammonia Oxidation, ACS Earth and Space Chemistry, 5, 1674–1685, https://doi.org/10.1021/acsearthspacechem.1c00021, 2021.

https://doi.org/10.5194/egusphere-2026-4245
Preprint. Discussion started: 10 August 2026

Pang, M., Jin, J., Segers, A., Lin, H.-X., Wang, G., Liao, H., and Han, W.: Zeeman: A Deep Learning Framework for Regional Atmospheric Chemistry Forecasting, Geophysical Research Letters, 53, e2025GL117 459, https://doi.org/10.1029/2025GL117459, e2025GL117459 2025GL117459, 2026.

Rijksdienst voor het Cultureel Erfgoed: Panorama Landschap, https://www.nationaalgeoregister.nl/geonetwork/srv/api/records/fbf78109-07e2-47aa-afe6-6ab813f3d4f7?language=all, 2026.

Shephard, M. W. and Cady-Pereira, K. E.: Cross-track Infrared Sounder (CrIS) satellite observations of tropospheric ammonia, Atmospheric Measurement Techniques, 8, 1323–1336, https://doi.org/10.5194/amt-8-1323-2015, 2015.

Shephard, M. W., Dammers, E., Cady-Pereira, K. E., Kharol, S. K., Thompson, J., Gainariu-Matz, Y., Zhang, J., McLinden, C. A., Kovachik, A., Moran, M., Bittman, S., Sioris, C. E., Griffin, D., Alvarado, M. J., Lonsdale, C., Savic-Jovcic, V., and Zheng, Q.: Ammonia measurements from space with the Cross-track Infrared Sounder: characteristics and applications, Atmospheric Chemistry and Physics, 20, 2277–2302, https://doi.org/10.5194/acp-20-2277-2020, 2020.

Sitwell, M.: EnsAI: An Emulator for Atmospheric Chemical Ensembles, https://arxiv.org/abs/2504.16024, 2026.

Van Damme, M., Whitburn, S., Clarisse, L., Clerbaux, C., Hurtmans, D., and Coheur, P.-F.: Version 2 of the IASI NH_3 neural network retrieval algorithm: near-real-time and reanalysed datasets, Atmospheric Measurement Techniques, 10, 4905–4914, https://doi.org/10.5194/amt-10-4905-2017, 2017.

van der Graaf, S., Dammers, E., Segers, A., Kranenburg, R., Schaap, M., Shephard, M. W., and Erisman, J. W.: Data assimilation of CrIS NH_3 satellite observations for improving spatiotemporal NH_3 distributions in LOTOS-EUROS, Atmospheric Chemistry and Physics, 22, 951–972, https://doi.org/10.5194/acp-22-951-2022, 2022.

van Zanten, M., Wichink Kruit, R., Hoogerbrugge, R., Van der Swaluw, E., and van Pul, W.: Trends in ammonia measurements in the Netherlands over the period 1993–2014, Atmospheric Environment, 148, 352–360, https://doi.org/10.1016/j.atmosenv.2016.11.007, 2017.

Wang, X., Tsimpidi, A. P., Luo, Z., Steil, B., Pozzer, A., Lelieveld, J., and Karydis, V. A.: The influence of ammonia emission inventories on size-resolved global atmospheric aerosol composition and acidity, Atmospheric Chemistry and Physics, 25, 10 559–10 586, https://doi.org/10.5194/acp-25-10559-2025, 2025.

White, E., Shephard, M. W., Cady-Pereira, K. E., Kharol, S. K., Ford, S., Dammers, E., Chow, E., Thiessen, N., Tobin, D., Quinn, G., O'Brien, J., and Bash, J.: Accounting for Non-Detects: Application to Satellite Ammonia Observations, Remote Sensing, 15, https://doi.org/10.3390/rs15102610, 2023.

Xia, J., Zhou, Y., Fang, L., Qi, Y., Li, D., Liao, H., and Jin, J.: South Asia anthropogenic ammonia emission inversion through assimilating IASI observations, Atmospheric Chemistry and Physics, 25, 7071–7086, https://doi.org/10.5194/acp-25-7071-2025, 2025.

Zeng, Z.-C., Lee, L., Qi, C., Clarisse, L., and Van Damme, M.: Optimal estimation retrieval of tropospheric ammonia from the Geostationary Interferometric Infrared Sounder on board FengYun-4B, Atmospheric Measurement Techniques, 16, 3693–3713, https://doi.org/10.5194/amt-16-3693-2023, 2023.